111公式章 1 节 1Piecewise damage model for SiC/SiC composites with multilevel experimental validation

Duoqi Shi [1], Zhenyu Wang [1], Changqi Liu [1,*], James Marrow [2], Xiaoguang Yang [1]

[1] School of Energy and Power Engineering, Beihang University, Beijing 100191, China

[2] Department of Materials, University of Oxford, Oxford OX1 3PH, UK

Abstract

Using multiscale and multidimensional data from experiments and advanced microscopic characterisation, a piecewise damage model for SiC/SiC composite structures has been proposed. First, the geometric information of the composite microstructure was acquired using scanning electron microscopy (SEM) and X-ray computed tomography (X-CT) and the microscopic and mesoscopic pores were characterised and measured. High-precision and total-factor finite element models were then established, and a piecewise damage model was introduced to the multilevel structures to simulate in detail the initiation and propagation of damage. Finally, in-situ experiments using the digital image correlation method were conducted to capture the strain fields of the SiC/SiC composites, validating the simulation results. After failure, the failure modes of the multilevel structures were observed and analysed by SEM and X-CT. In the piecewise damage model, observed failure modes (matrix cracking, interface debonding, fibre breakage, etc.) were associated within the progressive failure analysis concretely and the damage evolution

* Corresponding authors

E-mail address: lcqturbocae@buaa.edu.cn

were simulated accurately. Combining the multisource data during and after loading, the validity and reliability of this damage model based on failure mechanisms are demonstrated in the accurate prediction of the elastic and strength properties, deformation and stress fields in multilevel structures of SiC/SiC composites.

Keywords

A. Ceramic-matrix composites (CMCs); B. Strength; C. Damage mechanics; D. Mechanical testing

1. Introduction

The internal components of aeroengines operate under extremely severe service conditions, particularly at high temperatures, that restrict the applications of traditional metal materials[1][2][3]. Over the past three decades, significant progress has been made in the development of ceramic matrix composites (CMC) suitable for use at high temperatures[4][5][6], and some have been incorporated into the latest generation of aircraft engines[7][8][9][10]. Excellent thermal properties and low density make CMC attractive materials for several aeroengine components. However, the wider use of CMC remains limited, partly because of the lack of sufficiently validated and reliable modelling and testing methods for the deformation and failure analysis of structures.

Owing to the immature design and manufacturing methods for CMC structures, there are few components in applications, and many research studies have focused on the observation or prediction of the deformation and failure behaviours for these structures. For example, Patel et al. [11] conducted point-load-bending-static and fatigue tests to assess the strength of CMC combustor liners and observed typical failure modes on fracture surfaces under several stress states using a scanning electron microscope (SEM). Considering simplified geometric features, a few studies on deformation and failure analyses have been conducted for CMC specimens with notches or centre holes. Meyer et al. [12], Morscher et al. [13], and Delage et al [14]. conducted experimental strength measurements, crack characterisation, and fracture toughness analysis of notched specimens, respectively. In particular, Gao et al. [15] used a progressive failure analysis with the digital image correlation (DIC) method, and combined modelling and testing to study the strain field and damage evolution of specimens with a centre hole. The results indicated that the knowledge of the strain field was very relevant to CMC microstructures; however, the impact of microdefects was not considered.

The characteristics of CMC include multicomponent, inhomogeneous, and complex microstructures[16][17]. Some effective studies have used in-situ experiments with macro-micro characterisation. Bernachy-Barbe et al. [18] applied the DIC method to quantify the displacement field within the periodic patterns of woven SiC/SiC composites and connected the displacements to the stress and strain fields and crack opening and sliding behaviour. Zhang et al. [19] conducted in-situ experiments with

X-ray computed tomography (X-CT) on SiC/SiC composites to investigate the actual microstructures, initial porosity, and damage evolution with an increase in the tensile load. Han et al. [20] used SEM and X-CT to study the matrix cracking evolution of SiC/SiC composites under tensile loading and revealed a relationship between the microstructural features and crack propagation. Maillet et al. [21] coupled X-CT and acoustic emission (AE) to characterise the typical failure modes of SiC/SiC composites under in-plane tensile or flexural loading, namely, matrix cracking and fibre breakage. Liu et al. [22][23] combined X-CT, DIC and digital volume correlation (DVC) to conduct in-situ investigations on the flexural and compressive behaviours of SiC/SiC composites and fibre breakage resulting from buckling and shearing in the compressive area. X-CT and DVC have also been utilized to characterise the gradual propagation of matrix cracks in SiC/SiC composites under non-uniform loading, including hoop pressurisation [24][25][26]. and also to characterise fatigue damage [27]. In summary DIC and DVC can determine accurate physical quantities of displacement and strain in real time. X-CT provides a 3D depiction of the damage within the internal structure. SEM capturesthe failure modes on the fracture surfaces. Combining several characterisation methods in in-situ experiments is advantageous to establish the relationship between the physical quantities and damage evolution.

However, mechanical experiments on CMC are time-consuming and expensive. Based on the precision and total factor information from in-situ experiments of standard specimens, creating damage modelling approaches to analyse the

deformation and failure behaviours of CMC structures is necessary and effective[28]. For composites, existing damage models are typically developed from the microscale to the mesoscale and then to the macroscale [29][30][31][32][33]. For example, in resin matrix composites, Zheng et al. [34][35][36] adopted an exponential damage evolution law to capture the brittle fractures of yarns and employed a bilinear damage evolution law for the matrix. Both the laws were governed by the equivalent displacement, characteristic element length, and fracture energy density. He et al. [37][38][39] conducted mechanical experiments to calibrate the properties of the microscale constituents and proposed a multiscale elastic–plastic damage model to characterise the progressive failure behaviours of resin matrix composites. Generally, a solid foundation/of modelling and testing exists for the establishment of damage models to predict the mechanical behaviours of resin matrix composites [40][41][42][43]. This foundation also the main reference for modelling CMC damage. Shen et al. [44] constructed a mesoscopic model with the actual shape and position defects of SiC/SiC composites and calculated the tensile modulus and Poisson's ratio to be within 5% of the observed mechanical properties of the material. The predicted properties were primarily related to the microstructures and were independent of the failure modes. Wang et al. [45] imported a damage model verified using resin matrix composites and predicted the modulus of SiC/SiC composites under the influence of matrix cracks and fibre breakage under tensile loading. Chen et al. [46] analysed the effects of interface strength, fibre volume fraction and porosity in a phase-field model to predict the transverse and longitudinal tensile modulus and strength of

unidirectional SiC/SiC composites. Ikarashi et al. [47] developed a microdamage evolution model to predict the time-dependent deformation behaviour of SiC/SiC composites. However, the establishment of these models generally lacks sufficient support of test data, particularly for CMC. The complex braided structure and complete failure modes of CMC are not well considered in the modelling characterisation of the damage evolution of standard specimens. For CMC structures, modelling of deformation and failure behaviours is still an urgent and valuable problem. An clear demand exists for the development of a damage model, particularly for CMC that can be used for the deformation and failure analysis of multilevel structures, namely standard specimens, feature specimens, and structural components.

In the current study, a piecewise damage model for multilevel SiC/SiC composite structures is proposed, referring to multiscale and multidimensional data from accurate in-situ experiments and advanced microscopic characterisation techniques. High-precision and total factor geometric information of the composites was acquired using SEM and X-CT. The damage variables were accurately defined based on the test data from in-situ experiments of SiC/SiC composites, and the evolution laws were selected based on the damage characteristics of the SiC/SiC composites. At the macroscopic level, the damage evolution depending on the stress states was split into two levels to simulate the actual failure behaviour of the SiC/SiC composites. Subsequently, in-situ experiments with DIC were conducted to capture the strain fields of the multilevel structures. After failure, the failure modes of the composites were observed and classified using SEM and X-CT, and their influence was

adequately considered in the proposed damage model. These validated and reliable modelling and testing methods will serve as a foundation for the strength assessment and design of SiC/SiC composite structures.

2. Specimens and experiments

2.1 Specimens

Standard and feature specimens with central holes were investigated, as shown in Fig. 1 (a). Both were three-dimensional four-directional (3D4d) braided SiC/SiC composites fabricated via the precursor infiltration pyrolysis (PIP) process. The dimensions of each specimen were approximately 125mm×6mm×3mm (length×width×thickness). The diameter of the central hole was 1mm. The mechanical properties of SiC/SiC composites are primarily affected by pore dispersion in the matrix and fibre bundles during the fabrication process.[48][49][50][51]. To accurately reconstruct the pore features, the specimens were scanned using X-CT, as shown in Fig. 1 (b). These X-CT observations were obtained in a reconstructed volume of a cylinder of ~1700 voxels radius and 750 voxels height, with a voxel size of 3.5μm and 80keV X-ray energy. The observed pores can be categorised into five groups based on their volume and distinguished by a variety of colours. The largest pore, with a volume of 0.63mm^3, was directly visible at the macroscale. The pores with the lowest volume, measuring 25μm^3, were related to the microscale. Fig. 1 (c) shows the proportion of the pore volume distribution on a scale ranging from 1μm^3 to

1mm^3. The pores with a volume below 100μm^3 account for the highest percentage (66.5%) of the total observed porosity. For simulation precision, geometric models of SiC/SiC composites must be constructed with actual pore distributions across the length scales.

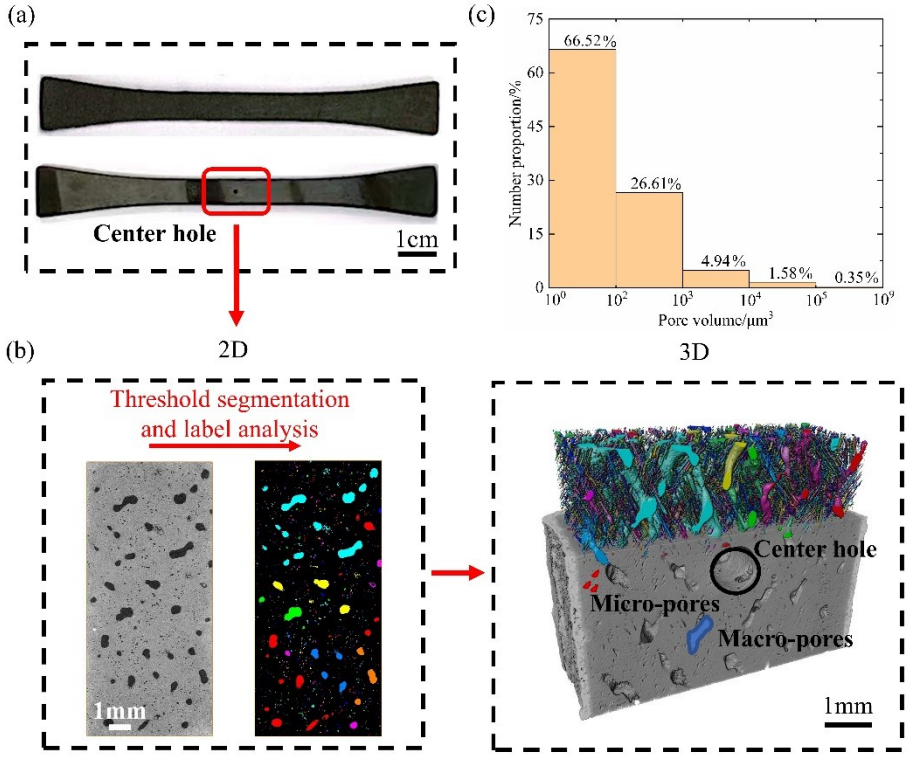


Fig. 1 (a) standard and feature specimens, (b) X-CT reconstruction of pore distribution in specimens, and (c) statistical results of pores

2.2 Experiments

In-situ experiments according to test standard ASME C1275 were conducted at room temperature using an Instron universal testing machine with DIC. The specimens were loaded at a speed of 0.3mm/min. A Daheng MER series camera captured images during the experiments at a sampling rate of 2Hz. Fig. 2 depicts the complete

experimental system used to perform the in-situ experiments using DIC at room temperature. The VIC-2D software was adopted to conduct the DIC analysis. For a higher computational accuracy of the strain, the size of DIC measurement area is twice of the unit cell size[52]. The region of interest was subdivided into uniform grids with a subset size of 21 × 21 pixels and a step size of 3 pixels. Additionally, the time delay between camera shooting and data gathering was less than 0.1s. The engineering strain of the specimens was measured using an extensometer at a standard gage lengthof 25mm to confirm the accuracy of the in-situ experiments with DIC.

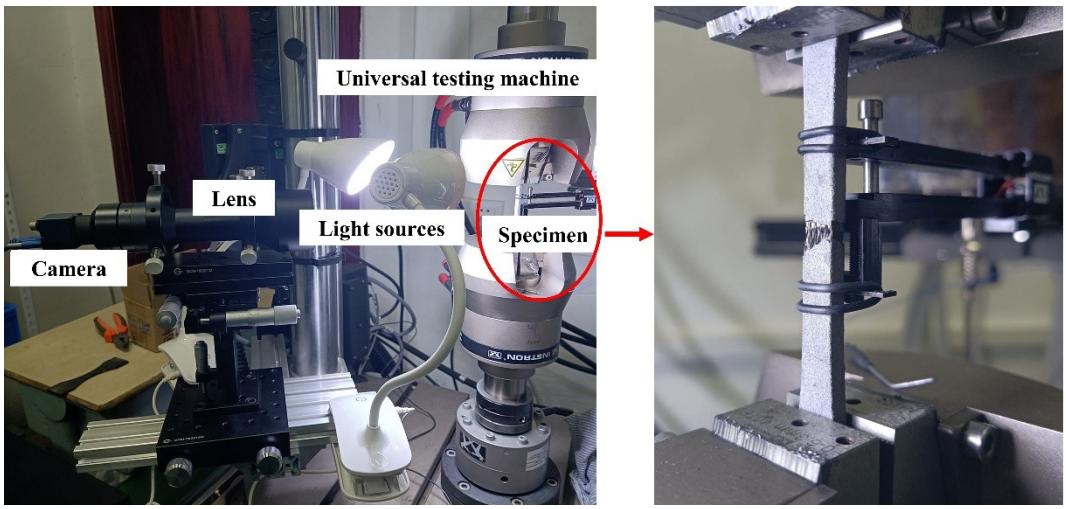


Fig. 2 Complete experimental systems used to perform the in-situ experiments using DIC at room temperature

Fig. 3 shows the application of X-CT for the geometric reconstruction and damage inspection of SiC/SiC composites. Before loading, several original images of the specimens were captured using the Zeiss Scout-and-Scan Control System with a voxel size of 3.5μm. 2D slices were reconstructed using the Zeiss XRM Reconstructor.

High-precision and total factor geometric information of the SiC/SiC composites was acquired by analysing slices of the reconstructed 3D dataset in the software ImageJ. The 3D images were visualised using Avizo software. The unloaded specimens, visualised in the same manner byX-CT after being mechanically tested to failure, clearly show the development of damage. Failure modes, such as debonding inter bundle, fibre breakage, and cracking intra bundle, were observed.

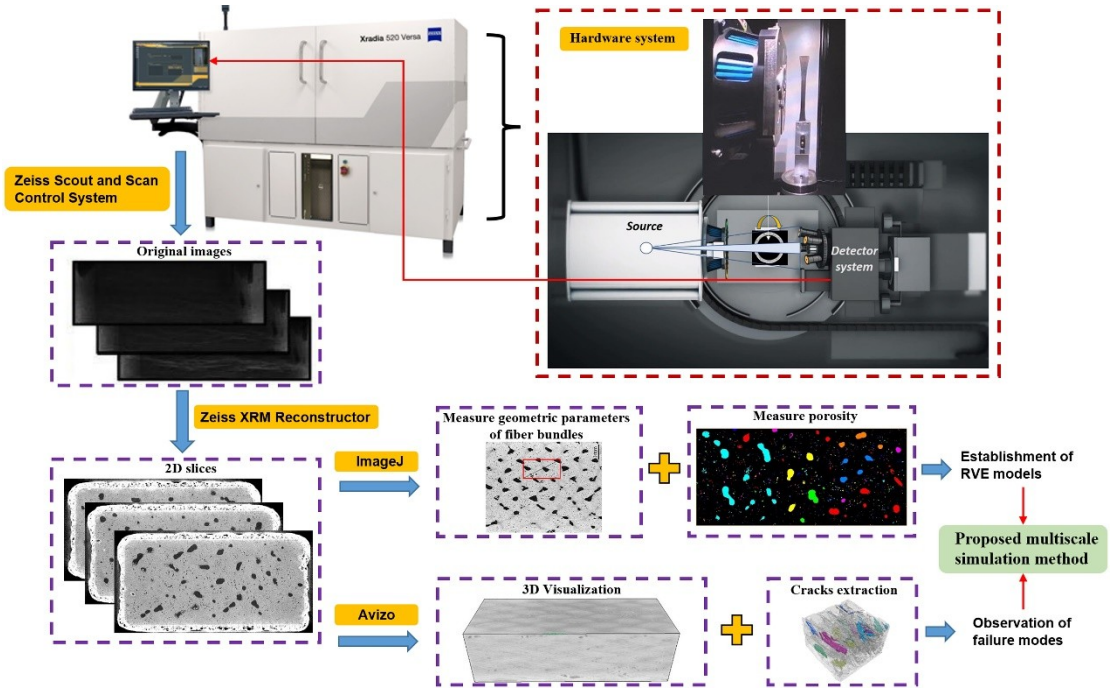


Fig. 3 The application of X-CT for the geometric reconstruction and damage inspection of SiC/SiC composites

3. Piecewise damage modelling

3.1 Multilevel structures

Fig. 4 shows the multilevel analysis of the high-precision and total factor geometric structures of the SiC/SiC composites. The mechanical properties, deformation, and failure behaviours of basic components, standard specimens, feature specimens, and structural components were investigated. Periodic representative volume elements (RVEs) of the SiC/SiC composites were constructed based on the periodic characteristics of the microscopic and mesoscopic structures[53][54].

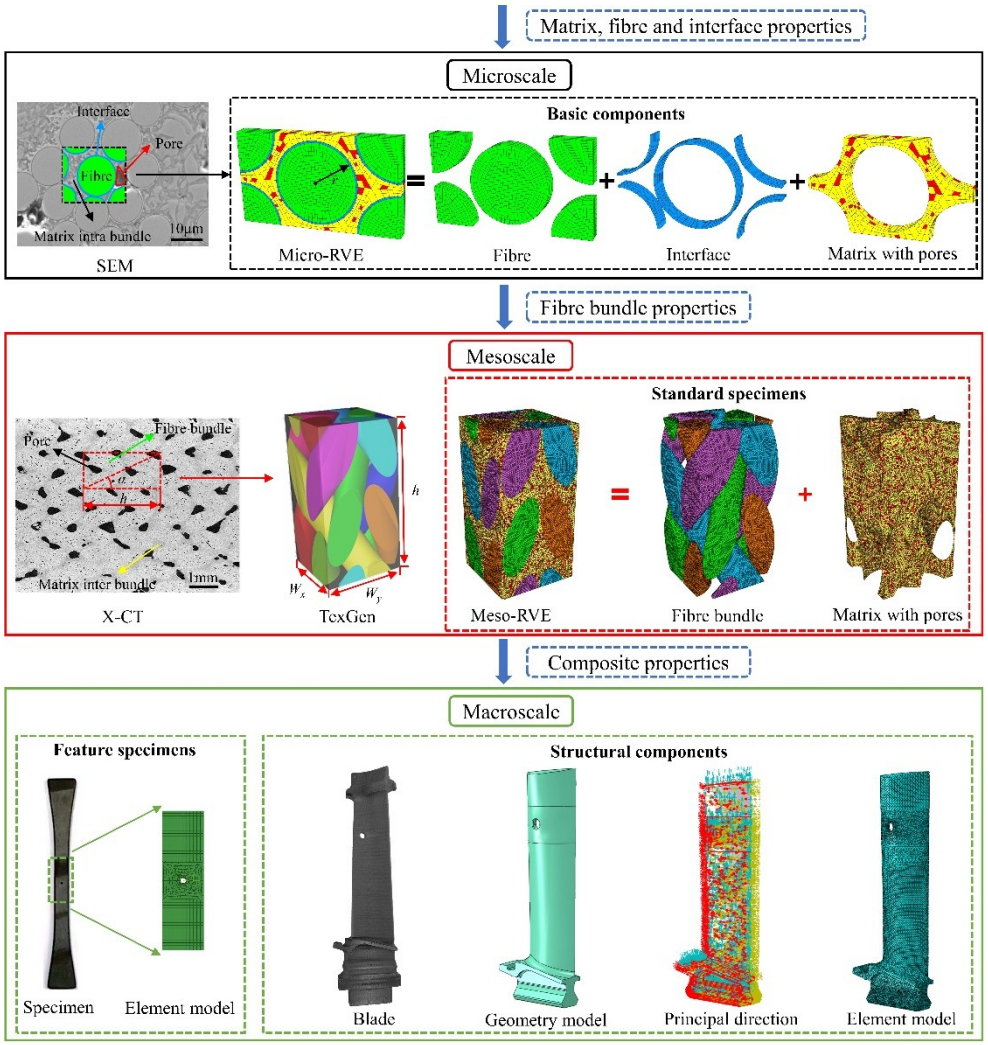


Fig. 4 Multilevel analysis of the high-precision and total-factor geometric structures of the SiC/SiC composites

SEM images of the SiC/SiC composites were obtained at the microscale to verify the geometric parameters of the fibre bundles. According to the manufacturing data, the fibre volume fraction V_f was 65%. Additionally, the fibre radius r (5μm) and interface thickness (0.05r) were defined. In the finite element analysis, C3D8 elements were used for the matrix and fibres, and COH3D8 elements were used as the interface. Considering that the pore defects were mainly distributed in the matrix, a Python

script was developed to generate the measured porosity of the fibre bundle. The tested composite porosity V_p on the microscale was 1.66%, the interface volume fraction V_i was approximately 6.67%, and fibre bundle fill factor ε was approximately 60.3%. The matrix porosity of the intra fibre bundles was calculated to be 9.67% using Eq. (1), and the actual pores are shown as red elements in the matrix.

$$V_{mp} = \frac{V_p}{\varepsilon\left(1 - V_f - V_i\right)} \quad 22\backslash * \text{ MERGEFORMAT ()}$$

At the mesoscale, a composite structure is typically divided into three types of RVEs (that is, interior, surface, and corner RVEs), and the interior RVEs occupy most of the composites[55][56]. Therefore, periodic interior RVEs were constructed to investigate the mechanical behaviour of the SiC/SiC composites. Moreover, the X-CT images were used to determine the braided patterns of the composites. For the 3D4d braided SiC/SiC composites, each interior RVE included 12 fibre bundles and 4 smaller fibre bundles. The fibre bundles were divided into four groups, depending on their orientation. The braided angle α and RVE height h were approximately 27° and 2.5mm, respectively. Other parameters (that is, length W_x, width W_y, interior braided angle γ, semi-major axis a, and semi-minor b of the oval fibre bundle section) were computed using Eq. (2). A Python script with geometric parameters was programmed and imported into the TexGen software to construct the mesoscopic RVE. Next, in the HyperMesh software, C3D4 elements were adopted in the finite element models.

$$\tan\alpha = \sqrt{2}\tan\gamma$$
$$h = \frac{\sqrt{2}W_x}{\tan\gamma} = \frac{\sqrt{2}W_y}{\tan\gamma}$$
$$W_x = W_y = 4\sqrt{2}b$$
$$h = \frac{8b}{\tan\gamma}$$

1 33* MERGEFORMAT ()

2 The tested composite porosity V_p at the mesoscale was 9.23%, and the matrix volume
3 fraction of inter fibre bundles was 1-ε. The matrix porosity V_{mp} of the inter fibre
4 bundles was computed as 23.43% using Eq. (3), and the pore elements were
5 constructed in the matrix.

$$V_{mp} = \frac{V_p}{1 - \varepsilon}$$

6 44* MERGEFORMAT ()

7 The periodic boundaries of the RVE at the microscale and mesoscale were defined
8 using the multiple point constraint equations described in Eq. (4). The EasyPBC plug-
9 in of the Abaqus software was used to increase efficiency with the constrained
10 boundary conditions[57].

$$X_{Front} - X_{Back} = Assignedvalue$$
$$X_{Top,Left} - X_{Bottom,Right} = 0$$
$$Y_{Top,Front,Left} - Y_{Bottom,Back,Right} = 0$$
$$Z_{Front,Top,Left} - Z_{Back,Bottom,Right} = 0$$

11 55* MERGEFORMAT ()

12 where *X*, *Y* and *Z* are displacement in three directions.

Additionally, the stress–strain curves of the RVE at the microscale and mesoscale were calculated using mean stress $\overline{\sigma}_{ij}$ and mean strain $\overline{\varepsilon}_{ij}$ of the RVE, as described in Eq. (5).

$$\overline{\sigma}_{ij} = \frac{1}{V}\int_V \sigma_{ij} dV = \frac{\sum_{k=1}^{n_e}\left(\sigma_{ij}^{e} V_k^{e}\right)}{\sum_{k=1}^{n_e} V_k^{e}}$$
$$\overline{\varepsilon}_{ij} = \frac{1}{V}\int_V \varepsilon_{ij} dV = \frac{\sum_{k=1}^{n_e}\left(\varepsilon_{ij}^{e} V_k^{e}\right)}{\sum_{k=1}^{n_e} V_k^{e}} \quad 66\text{* MERGEFORMAT ()}$$

On the macroscale, the size of gauge section in feature specimens with a centre hole was 10.1mm×1.2mm×30mm. C3D8R elements were used in the finite element analysis. Simple boundary conditions were adopted. One side was fixed, and a displacement-controlled load was applied to the other side. Furthermore, the low-pressure turbine blade in a mature turbojet was connected to the geometric structure of the structural components[58]. The blade root was modified to a dovetail root, and C3D4 finite elements were used for the blade. A local coordinate system was built at the interface between the dovetail root and the blade disk, and the interface displacement was limited. Several locations on the bottom surface of the root were restricted in circumferential and longitudinal displacements. The centrifugal load was applied that was equivalent to a rotational speed of 11440 rpm.

3.2 Material properties

On the microscale, the matrix and fibre are considered as isotropic materials for efficient modelling. Cohesive elements were used to define the constitutive response of the interface using a traction-separation law[59]. The mechanical properties of these basic components are listed in Table. 1. Subscript ‘1’ denotes the longitudinal direction of the fibre bundles and ‘2’ and ‘3’ denote their transverse direction. Considering the significant impact of pore defects on the matrix properties, the modulus and strength of the matrix were corrected using Eq. (6) and (7) with the matrix porosity V_{mp} of the intra fibre bundles.

Table 1 The mechanical properties of constituents of fibre bundles

SiC fibre								
E_{11}(GPa)	E_{22}(GPa)	E_{33}(GPa)	G_{12}(GPa)	G_{23}(GPa)	G_{31}(GPa)	v_{12}	v_{23}	v_{31}
260	260	260	108.3	108.3	108.3	0.2	0.2	0.2
T_{11}(MPa)	C_{11}(MPa)							
2500	1800							
SiC matrix (intra bundle)								
E(GPa)	μ	T(MPa)	C(MPa)	S(MPa)				
82.5	0.3	114	228	57				
Interface[60]								
k_{nn} (N/mm^3)	k_{ss} (N/mm^3)	k_{tt} (N/mm^3)	t_n^0(MPa)	t_s^0(MPa)	t_t^0(MPa)	G_n^C(N/mm)	G_s^C(N/mm)	G_t^C(N/mm)
10^5	10^5	10^5	89	89	89	0.3	0.6	0.6

For elastic modulus[61],

$$E_{mp} = E_m\left(1 - f_1 V_{mp} - f_2 V_{mp}^2\right) \quad 77\backslash * \text{ MERGEFORMAT ()}$$

where E_{mp} is the elastic modulus of matrix with pores, E_m is the elastic modulus of the matrix, and f_1 and f_2 are constants as 1.9 and 0.9 while the Poisson ratio of the ceramic matrix is 0.3.

For strength[62],

$$S_{mp} = S_m \left[1 - \sqrt{\frac{4V_{mp}}{\pi}} \right] \quad 88\backslash* \text{ MERGEFORMAT ()}$$

where S_{mp} is the strength of the matrix with pores, and S_m is the strength of the matrix.

The mechanical properties of the fibre bundles were acquired from the microscopic simulations in this study and imported into the mesoscopic model. The mechanical properties of the fibre bundles and matrix are listed in Table 2. At the mesoscale, the matrix inter fibre bundles were also considered as isotropic materials. The modulus and strength of the matrix were corrected using Eq. (6) and (7) with the matrix porosity V_{mp} of the inter fibre bundles. The fibre bundles were modelled as unidirectional materials with transverse isotropic properties. The torsion of fibre bundles during the braiding process influenced their properties, particularly the longitudinal tensile elastic modulus and strength. These values were corrected using Eq. (8)[63][64].

$$E_{11t} = E_{11} \cos^2 \theta$$
$$T_{11t} = \frac{T_{11} S_{12}}{\cos \theta \sqrt{S_{12}^2 \cos^2 \theta + T_{11}^2 \sin^2 \theta}} \quad 99\backslash* \text{ MERGEFORMAT ()}$$

where E_{11t} and T_{11t} are the elastic modulus and strength with torsion influence, θ is torsion angle, measured at 6°.

Table 2 The mechanical properties of fibre bundles and matrix inter bundle

SiC/SiC fibre bundle								
E_{11}(GPa)	E_{22}(GPa)	E_{33}(GPa)	G_{12}(GPa)	G_{23}(GPa)	G_{31}(GPa)	v_{12}	v_{23}	v_{31}
195.6	165.2	165.2	69.3	67.9	69.3	0.228	0.266	0.228
T_{11}(MPa)	C_{11}(MPa)	T_{22}(MPa)	C_{22}(MPa)	T_{33}(MPa)	C_{33}(MPa)	S_{12}(MPa)	S_{23}(MPa)	S_{31}(MPa)
1682.6	1212.3	83.6	170.5	83.6	170.5	61.6	56.2	61.6
SiC matrix (inter bundle)								
E(GPa)	μ	T(MPa)	C(MPa)	S(MPa)				
60.4	0.3	80	160	40				

Under a longitudinal compressive load, the failure modes of the fibre bundles were typically related to interface debonding and fibre buckling[65]. The longitudinal compressive strength of the fibre bundle was less than C_{11} calculated in the microscopic simulation. The strength of the fibre bundles was corrected using Eq. (20).

$$C_{11d} = 10S_{12} + 2.5T_m$$
$$C_{11b} = \frac{C_m}{1 - V_{fb}\left(1 - G_m / G_{f12}\right)} \quad (1010\text{* MERGEFORMAT ()})$$

where T_m, C_m, and G_m denote the tensile strength, compressive strength, and shear modulus, respectively, of the matrix intra fibre bundles, and G_{f12} denotes the longitudinal shear modulus of the fibre. C_{11d} was adopted with interface debonding, and C_{11b} was used with fibre buckling. In the mesoscopic modelling in this study, C_{11} was corrected to the average values of C_{11d} and C_{11b}.

Based on the mesoscopic simulation, the mechanical properties of the SiC/SiC composites were input into the macroscopic model and are presented in Table 3. At the macroscale, the composites were modelled as unidirectional materials with transversely isotropic properties. Subscript '1' denotes the longitudinal direction of composites and '2' and '3' denote their transverse directions. The density of the composites was 2.18g/cm^3. The primary direction of the composites in the blade was determined using a local coordinate system, assuming that the braiding direction in the blade was consistent. In Fig. 4, the blue direction (1) represents both the longitudinal direction of the composite and radial direction of the blade.

Table 3 The mechanical properties of SiC/SiC composites at room temperature

3D four-directional braided SiC/SiC composites								
E_{11}(GPa)	E_{22}(GPa)	E_{33}(GPa)	G_{12}(GPa)	G_{23}(GPa)	G_{31}(GPa)	v_{12}	v_{23}	v_{31}
121.3	105.2	105.2	48.5	46.9	48.5	0.26	0.22	0.26
T_{11}(MPa)	C_{11}(MPa)	T_{22}(MPa)	C_{22}(MPa)	T_{33}(MPa)	C_{33}(MPa)	S_{12}(MPa)	S_{23}(MPa)	S_{31}(MPa)
336.2	205.0	110.5	153.6	110.5	153.6	55.8	51.6	55.8
PLS(MPa)								
85								

3.3 Progressive failure analysis

Progressive failure analysis (PFA) is an efficient approach to analyse the failure behaviour of composite materials[66][67][68][69]. Flowcharts of the PFA for the SiC/SiC composites are illustrated in Fig. 5. In addition to stress analysis, failure analysis, and material degradation, multilevel structures and corrected material parameters, particularly for SiC/SiC composites, were imported into the PFA. Fig. 6 shows the selection of damage initiation criteria and damage evolution laws in the damage

model based on the damage characteristics of the SiC/SiC composites. Several parameters in the damage initiation criteria were selected from the measurable data in the experiments on SiC/SiC composites. The damage model revealed the failure behaviour under various loading states. Additionally, the mechanical properties, strength prediction, stress, and strain fields of multilevel structures were obtained in the PFA.

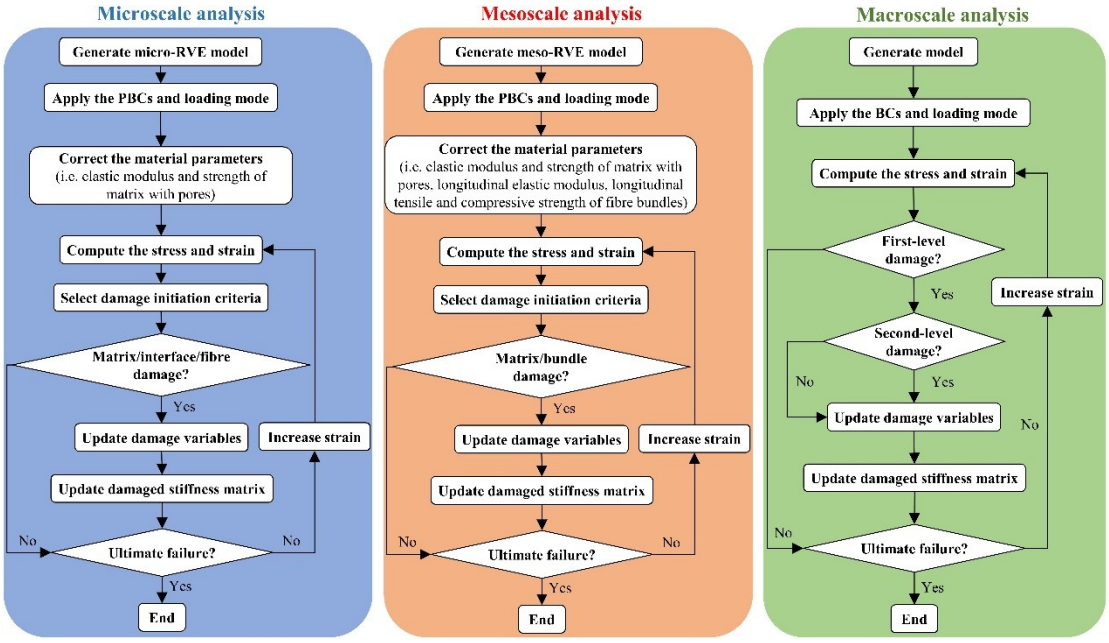


Fig. 5 Flowcharts of the PFA for SiC/SiC composites

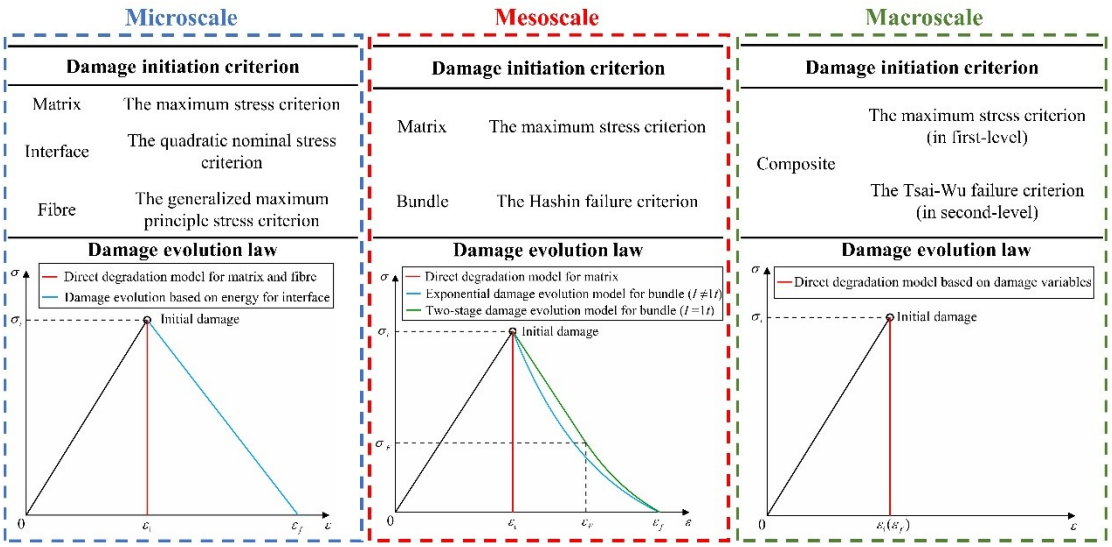


Fig. 6 The selection of damage initiation criteria and damage evolution laws in the piecewise damage model

3.3.1 Microscopic damage model

In the damage model, the damage initiation criteria were first selected. Typically, the failure behaviour of fibres depends on the longitudinal loads, and the section of the fibres is perpendicular to or barely oblique to the axis[70]. Only the longitudinal tensile and compressive strengths could be assessed in the experiments on the SiC/SiC composites. Therefore, the generalised maximum principal stress criterion was used to determine the initial damage to the fibre. In addition, the maximum stress criterion was adopted for the matrix, and the quadratic nominal stress criterion was applied to the cohesive elements to determine the initial damage. The damage initiation criteria can be expressed as follows:

For the fibre,

$$\sigma_{eq} \geq T_{11}$$

$$\sigma_{eq} = \begin{cases} \sigma_1, \ \sigma_3 < 0 \\ \left[(\sigma_1)^q + (\sigma_2)^q \right]^{\frac{1}{q}}, \ \sigma_3 = 0 \\ \left[(\sigma_1)^q + (\sigma_2)^q + (\sigma_3)^q \right]^{\frac{1}{q}}, \ \sigma^3 > 0 \end{cases} \quad 1111\text{* MERGEFORMAT}$$

()

$$\sigma_{eq} \leq -C_{11}$$

$$\sigma_{eq} = \begin{cases} \sigma_3, \sigma_1 > 0 \\ \sigma_3 - \sigma_1, \sigma_1 \leq 0 \end{cases} \quad 1212\text{* MERGEFORMAT ()}$$

where T_{11} and C_{11} denote the longitudinal tensile and compressive strengths, respectively; σ_1, σ_2, and σ_3 denote the principal stresses; σ_{eq} denotes the equivalent stress; and q denotes the empirical parameter whose value is 3. When Eq. (10) is satisfied, the tensile failure occurs in the longitudinal direction, and when Eq. (11) is satisfied, the compression failure occurs in the longitudinal direction.

For the matrix,

$$\begin{aligned} &\sigma_1 \geq T \\ &\sigma_1 - \sigma_3 \geq S \\ &\sigma_3 \leq -C \end{aligned} \quad 1313\text{* MERGEFORMAT ()}$$

where T, C, and S denote the tensile, compressive, and shear strengths, respectively. In Eq. (12), the failure corresponding to the satisfied equation, occurs.

For the interface[71],

$$\langle t_n \rangle = \frac{|t_n| + t_n}{2}$$

$$\left(\frac{\langle t_n \rangle}{t_n^0}\right)^2 + \left(\frac{t_s}{t_s^0}\right)^2 + \left(\frac{t_t}{t_t^0}\right)^2 = 1 \quad (14)$$

where t_n, t_s and t_t denote nominal stress; t_n^0, t_s^0 and t_t^0 denote strength in the normal, the first and the second shear directions on the interface, respectively.

When the stress state in the elements satisfied the damage initiation criteria, the failure occurred via the defined failure modes. Moreover, stiffness steadily deteriorated in accordance with the damage evolution laws. The relationship between stress **σ** and strain **ε** can be described as follows:

$$\boldsymbol{\sigma} = \mathbf{C}_d : \boldsymbol{\varepsilon} \quad (15)$$

where $\mathbf{C}_d$ represents the damaged stiffness matrix.

When the fibre and matrix were damaged, a direct degradation model was utilised to compute the stiffness of the damaged elements. For the matrix, E decreased by 90%, and μ remained unchanged. For the fibres, E_{11} and G_{12} decreased by 90%, whereas the other parameters remained unchanged.

For the matrix, damaged stiffness matrix $\mathbf{C}_d$ can be written as follows:

$$\mathbf{C}_{\mathrm{d}}=\begin{bmatrix} 0.1c_{11} & & & & & \\ 0.1c_{12} & 0.1c_{22} & & & sym & \\ 0.1c_{13} & 0.1c_{23} & 0.1c_{33} & & & \\ 0 & 0 & 0 & 0.1c_{44} & & \\ 0 & 0 & 0 & 0 & 0.1c_{55} & \\ 0 & 0 & 0 & 0 & 0 & 0.1c_{66} \end{bmatrix} \quad (16)$$

MERGEFORMAT ()

For the interface, a bilinear constitutive relation was determined to describe the constitutive responses before and after failure in the cohesive elements. Before failure, the linear constitutive relation can be expressed by Eq. (16).

$$\mathbf{t}=\begin{bmatrix} t_n \\ t_s \\ t_t \end{bmatrix}=\begin{bmatrix} k_{nn} & 0 & 0 \\ 0 & k_{ss} & 0 \\ 0 & 0 & k_{tt} \end{bmatrix}\begin{bmatrix} \delta_n \\ \delta_s \\ \delta_t \end{bmatrix}=\mathbf{K}:\boldsymbol{\delta}=\mathbf{C}:\boldsymbol{\varepsilon} \quad (17)$$

MERGEFORMAT ()

where **t** denotes the nominal stress, **C** denotes the stiffness matrix, **ε** denotes the nominal strain, **K** and **δ** denote the stiffness matrix and displacement by orthogonal transformation, respectively, and k_{nn}, k_{ss}, and k_{tt} denote the stiffness parameters in **K**. With constant thickness T_0=1, nominal strain components were equal to respective components of relative displacement (δ_n, δ_s, and δ_t) between top and bottom of the cohesive layer.

The damage evolution law for the interface is based on the fracture energy. It was assumed that the critical fracture energies in the first and second shear directions were the same, and the Benzeggagh–Kenane fracture criterion was adopted to define the

critical fracture energy G^C in the degradation process[72]. This criterion is given by Eq. (17).

$$\begin{aligned} G_s^C &= G_t^C \\ G_n^C + \left(G_s^C - G_n^C\right)\left\{\frac{G_S}{G_T}\right\}^{\eta} &= G^C \\ G_S &= G_s + G_t \\ G_T &= G_n + G_S \end{aligned} \qquad (1818\backslash * \text{ MERGEFORMAT }())$$

where G_n^C, G_s^C, and G_t^C denote the critical fracture energies in the normal, first, and second shear directions on the interface, respectively; G_n, G_s, and G_t denote the fracture energies in the specified directions and these are described as the area under the nominal stress **t** -displacement **δ** curve in a traction-separation description; and η denotes the material parameter, defined as 1.

After failure, the linear constitutive relationship can be expressed by Eq. (18).

$$\begin{aligned} t_n &= \begin{cases} (1-d)\,\bar{t}_n & \bar{t}_n \geq 0 \\ \bar{t}_n & \bar{t}_n < 0 \end{cases} \\ t_s &= (1-d)\,\bar{t}_s \\ t_t &= (1-d)\,\bar{t}_t \end{aligned} \qquad (1919\backslash * \text{ MERGEFORMAT }())$$

where $\bar{t}_n$, $\bar{t}_s$, and $\bar{t}_t$ denote the corresponding nominal stresses of the same displacement before failure, and d denotes the damage variable and can be computed as in Eq. (19).

$$d = \frac{\delta_m^{\,f}(\delta_m^{\max} - \delta_m^{\,0})}{\delta_m^{\max}(\delta_m^{\,f} - \delta_m^{\,0})}$$
$$\delta_m^{\,f} = \frac{2G^C}{T_{eff}^{\,0}}$$

2020* MERGEFORMAT ()

where $T_{eff}^{\,0}$ denotes the effective traction at initial damage, and δ_m denotes the effective displacement defined as follows:

$$\langle \delta_n \rangle = \frac{|\delta_n| + \delta_n}{2}$$
$$\delta_m = \sqrt{\langle \delta_n \rangle^2 + \delta_s^{\,2} + \delta_t^{\,2}}$$

2121* MERGEFORMAT ()

where $\delta_m^{\,f}$ and $\delta_m^{\,0}$ denote the effective displacements at the ultimate failure and initial damage, respectively, and $\delta_m^{\max}$ denotes the maximum value of the effective displacement attained under loading.

3.3.2 Mesoscopic damage model

For the matrix inter fibre bundles, the maximum stress criterion was also adopted as the damage initiation criterion, and the direct reduction method for the matrix was used as the damage evolution law. Considering the tensile and compressive failure modes of different components, the Hashin failure criterion has been widely used to predict unidirectional composite failures[73]. Therefore, the 3D Hashin failure criterion was adopted for fibre bundles as the damage initiation criterion. It can be expressed as follows:

1 Tensile failure mode of the fibre

$$\sigma_{11} > 0$$

$$f_{1t} = \sqrt{\frac{\sigma_{11}^{\ 2}}{S_{11}^{\ 2}} + \frac{\left(\tau_{12}^{\ 2} + \tau_{13}^{\ 2}\right)}{S_{12}^{\ 2}}}$$

2 2222* MERGEFORMAT ()

3 Compressive failure mode of the fibre

$$\sigma_{11} < 0$$

$$f_{1c} = \sqrt{\left(\frac{\sigma_{11}}{C_{11}}\right)^2}$$

4 2323* MERGEFORMAT ()

5 Tensile failure mode of the matrix intra bundle

$$\sigma_{22} + \sigma_{33} \geq 0$$

$$f_{2(3)t} = \sqrt{\frac{\left(\sigma_{22} + \sigma_{33}\right)^2}{T_{22}^{\ 2}} + \frac{\left(\sigma_{23}^{\ 2} - \sigma_{22}\sigma_{33}\right)}{S_{23}^{\ 2}} + \frac{\left(\sigma_{12}^{\ 2} + \sigma_{13}^{\ 2}\right)}{S_{12}^{\ 2}}}$$

6 2424*

7 MERGEFORMAT ()

8 Compressive failure mode of the matrix intra bundle

$$\sigma_{22} + \sigma_{33} \leq 0$$

$$f_{2(3)c} = \sqrt{\left[\left(\frac{C_{22}}{2S_{23}}\right)^2 - 1\right]\frac{\sigma_{22} + \sigma_{33}}{C_{22}} + \frac{\left(\sigma_{22} + \sigma_{33}\right)^2}{4S_{23}^{\ 2}} + \frac{\left(\sigma_{23}^{\ 2} - \sigma_{22}\sigma_{33}\right)}{S_{23}^{\ 2}} + \frac{\left(\sigma_{12}^{\ 2} + \sigma_{13}^{\ 2}\right)}{S_{12}^{\ 2}}}$$

9 2525*

10 MERGEFORMAT ()

where f_I denotes the damage initiation parameter related to the failure mode; σ denotes the stress; and T, C, and S denote the tensile, compressive, and shear strengths of fibre bundles, respectively. Subscripts 't' and 'c' represent the tensile and compressive loading states, respectively.

With the exception of longitudinal tensile loading, the exponential damage evolution law was used to predict stiffness degeneration as follows:

$$d_I = 1 - \frac{1}{f_I}\exp\left[A_I(1 - f_I)\right] \qquad (I = 1c, 2(3)t, 2(3)c)$$

2626* MERGEFORMAT ()

where d_I denotes the damage variable related to the failure mode, and A_I denotes the exponential damage softening coefficient defined as in Eq. (26)[74].

$$A_I = \frac{2LS_I^2}{2E_I G_I - LS_I^2}$$

2727* MERGEFORMAT ()

where L denotes the element characteristic length, and S_I, E_I, and G_I denote the strength, elastic modulus, and fracture energy of the unit area, respectively.

To describe matrix cracking of the intra fibre bundles and fibre pull-outs under a longitudinal tensile load, the linear and exponential damage evolution laws were combined to predict the fibre bundle stiffness degeneration as follows:

$$d_{1t} = 1 - \frac{1 - d_{1t}^{L}}{f_{1t}^{E}} \exp\left[A_{1t} \left(1 - f_{1t}^{E} \right) \right] \tag{2828}$$

where d_{1t} denotes the longitudinal tensile damage variable, A_{1t} denotes the exponential damage softening coefficient under a longitudinal tensile load, and d_{1t}^{L} and f_{1t}^{E} denote auxiliary damage variables defined as in Eq. (28).

$$\begin{aligned} d_{1t}^{L} &= 1 + \frac{K_{1t}}{E_{11}} - \left(1 + \frac{K_{1t}}{E_{11}} \right) \frac{1}{f_{1t}^{L}} \\ f_{1t}^{L} &= \max\left(1, \min\left(f_{1t}, f_{1t}^{F} \right) \right) \\ f_{1t}^{E} &= \max\left\{ 1, \left(1 - d_{1t}^{F} \right) \frac{T_{11}}{S_{PO}} f_{1t} \right\} \end{aligned} \tag{2929}$$

where K_{1t} denotes the slope in the linear softening segment, f_{1t}^{L} denotes the auxiliary damage threshold, f_{1t}^{F} denotes the damage threshold at the transition point between linear and exponential softening, and d_{1t}^{F} and S_{PO} denote the corresponding damage variables and stress, respectively. These parameters can be defined as in Eq. (29).

$$\begin{aligned} K_{1t} &= \frac{L T_{11} E_{11} \left(T_{11} - S_{PO} \right)}{2 G_{1t}^{L} E_{11} - L T_{11} \left(T_{11} - S_{PO} \right)} \\ f_{1t}^{F} &= 1 + \frac{E_{11}}{K_{1t}} \left(1 - \frac{S_{PO}}{T_{11}} \right) \\ d_{1t}^{F} &= 1 + \frac{K_{1t}}{E_{11}} - \frac{1}{f_{1t}^{F}} \left(\frac{E_{11}}{K_{1t}} + 1 \right) \\ A_{1t} &= \frac{2 L S_{PO}^{2}}{2 \left(1 - d_{1t}^{F} \right) E_{11} G_{1t}^{E} - L S_{PO}^{2}} \end{aligned} \tag{3030}$$

where G_{1t}^{L} and G_{1t}^{E} denote the fracture energies per unit area at the linear and exponential softening segments, respectively.

To express the damage evolution law for the fibre bundles under longitudinal tensile loading, d_{1t} can be written as in Eq. (30).

$$d_{1t}=\begin{cases}1+\dfrac{K_{1t}}{E_{11}}-\left(1+\dfrac{K_{1t}}{E_{11}}\right)\dfrac{1}{f_{1t}} & \left(1\le f_{1t}\le f_{1t}^{F}\right)\\ 1-\dfrac{1-\left[1+\dfrac{K_{1t}}{E_{11}}-\left(1+\dfrac{K_{1t}}{E_{11}}\right)\dfrac{1}{f_{1t}^{F}}\right]}{\left(1-d_{1t}^{F}\right)\dfrac{T_{11}}{S_{PO}}f_{1t}}\exp\left\{A_{1t}\left[1-\left(1-d_{1t}^{F}\right)\dfrac{T_{11}}{S_{PO}}f_{1t}\right]\right\} & \left(f_{1t}>f_{1t}^{F}\right)\end{cases} \quad (3131)$$

* MERGEFORMAT ()

where S_{PO}, G_{1t}^{L}, and G_{1t}^{E} are defined, and the other parameters can be computed using Eq. (29). G_{1t}^{L} and G_I (I=2(3)t, 2(3)c) are related to matrix fracture energy G_m. G_{1t}^{E} and G_{1c} are related to fibre fracture energy G_f.

For fibre bundles, the damaged stiffness matrix $\mathbf{C_d}$ can be expressed using damage variables as follows:

$$\mathbf{C}_{\mathbf{d}}=\begin{bmatrix} b_f^{\,2}c_{11} & & & & & \\ b_f b_m c_{12} & b_m^{\,2}c_{22} & & & sym & \\ b_f b_m c_{13} & b_m^{\,2}c_{23} & b_m^{\,2}c_{33} & & & \\ 0 & 0 & 0 & b_f b_m c_{44} & & \\ 0 & 0 & 0 & 0 & b_f b_m c_{55} & \\ 0 & 0 & 0 & 0 & 0 & b_m^{\,2}c_{66} \end{bmatrix} \quad (3232)$$

* MERGEFORMAT ()

where b_f=1-d_1, and b_m=1-$d_{2(3)}$.

3.3.3 Macroscopic damage model

Based on the failure modes of the SiC/SiC composites, the damage initiation criteria were divided into two levels according to the stress state. At the first level, the maximum stress criterion was adopted to determine whether the stress state reached the proportional limit stress (PLS). The PLS is defined as the stress value at the end of the linear segment in the macroscopic stress–strain curve, approximately 85MPa at room temperature. At the second level, the Tsai–Wu failure criterion was used to determine whether a failure has occurred.

The 3D Tsai-Wu failure criterion can be expressed as follows:

$$F_1\sigma_{11}+F_2\sigma_{22}+F_3\sigma_{33}+F_{11}\sigma_{11}^{\ 2}+F_{22}\sigma_{22}^{\ 2}+F_{33}\sigma_{33}^{\ 2}+F_{44}\tau_{12}^{\ 2}+F_{55}\tau_{23}^{\ 2}+F_{66}\tau_{31}^{\ 2}$$
$$+2F_{12}\sigma_{11}\sigma_{22}+2F_{23}\sigma_{22}\sigma_{33}+2F_{31}\sigma_{33}\sigma_{11}=1 \quad (3333)$$

* MERGEFORMAT ()

where

$$\begin{cases} F_1=\dfrac{1}{T_{11}}-\dfrac{1}{C_{11}} & F_2=\dfrac{1}{T_{22}}-\dfrac{1}{C_{22}} & F_3=\dfrac{1}{T_{33}}-\dfrac{1}{C_{33}} \\ F_{11}=\dfrac{1}{T_{11}C_{11}} & F_{22}=\dfrac{1}{T_{22}C_{22}} & F_{33}=\dfrac{1}{T_{33}C_{33}} \\ F_{44}=\dfrac{1}{S_{12}^{\ 2}} & F_{55}=\dfrac{1}{S_{23}^{\ 2}} & F_{66}=\dfrac{1}{S_{31}^{\ 2}} \\ F_{12}=-\dfrac{1}{2}\sqrt{F_{11}F_{22}} & F_{23}=-\dfrac{1}{2}\sqrt{F_{22}F_{33}} & F_{31}=-\dfrac{1}{2}\sqrt{F_{33}F_{11}} \end{cases} \quad (3434)$$

* MERGEFORMAT ()

where T, C, and S denote the tensile, compressive, and shear strengths of the SiC/SiC composite, respectively.

In Eq. (32), the Tsai–Wu failure criterion exhibits a unified expression in an arbitrary loading state. To distinguish the different failure modes, parameters H_i (i=1, 2, …, 6) were introduced in Eq. (34).

$$\begin{aligned} H_1 &= F_{11}\sigma_{11}^{\ 2} \quad H_2 = F_{22}\sigma_{22}^{\ 2} \\ H_3 &= F_{33}\sigma_{33}^{\ 2} \quad H_4 = F_{44}\tau_{12}^{\ 2} \\ H_5 &= F_{55}\tau_{23}^{\ 2} \quad H_6 = F_{66}\tau_{31}^{\ 2} \end{aligned} \tag{3535* MERGEFORMAT ()}$$

When the stress state satisfies the damage initiation criteria in Eq. (32), the maximum parameter H_i indicates the principal failure mode. H_1, H_2, and H_3 express tensile and compressive damage in the longitudinal and transverse directions, and H_4, H_5, and H_6 express shear damage in the planes.

For SiC/SiC composites, the damaged stiffness matrix $\mathbf{C_d}$ can be expressed by the damage variables as follows:

$$\mathbf{C}_{\mathrm{d}} = \begin{bmatrix} b_0 b_1^{\ 2} c_{11} & & & & & \\ b_0 b_1 b_2 c_{12} & b_0 b_2^{\ 2} c_{22} & & & sym & \\ b_0 b_1 b_3 c_{13} & b_0 b_2 b_3 c_{23} & b_0 b_3^{\ 2} c_{33} & & & \\ 0 & 0 & 0 & b_0 b_4^{\ 2} c_{44} & & \\ 0 & 0 & 0 & 0 & b_0 b_5^{\ 2} c_{55} & \\ 0 & 0 & 0 & 0 & 0 & b_0 b_6^{\ 2} c_{66} \end{bmatrix} \tag{3636* MERGEFORMAT ()}$$

where b_i=1-D_i (i=0, 1, …, 6). D_0 expressed the damage related to the PLS at the first level, and its value was defined as 0.65. D_i (i=1, 2, …, 6) characterized the damage of the different failure modes at the second level, and its value was defined as 0.9.

4. Results and discussions

84.1 Experiment results

The macroscopic stress–strain curves and fracture surfaces of the standard specimens (that is, T1, T2, and T3) and feature specimens (that is, TH1, TH2, TH3, and TH4) under a tensile load, including the DIC and extensometer test results, are shown in Fig. 7. The DIC test results reportthe Lagrange strain, and the extensometer test results report the engineering strain. Therefore, the DIC test results were transformed into engineering strain using Eq. (36) and compared with the extensometer test results.

$$\sqrt{2e_L+1}-1=e_E \qquad 3737\text{* MERGEFORMAT ()}$$

where e_L denotes the Lagrange strain, and e_E denotes the engineering strain. The stress–strain curves obtained with DIC were consistent with those of the extensometer test results, proving the correctness of the DIC measurements. The PLS of standard specimens was 80~90MPa at room temperature. The ultimate tensile stress (UTS) is defined as the stress value at the breakpoint in the stress–strain curve of the

composites. The UTS of the standard specimens was 316~350MPa and that of the feature specimens was 200~270MPa at room temperature.

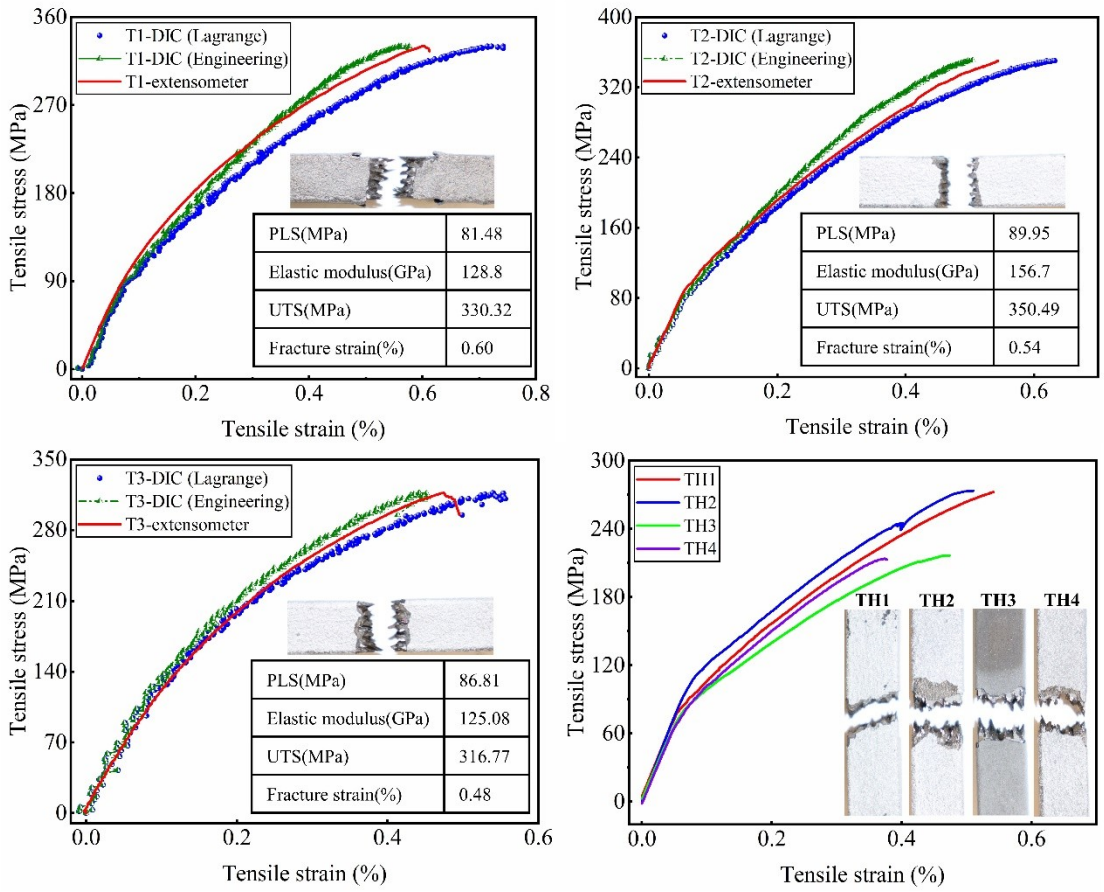


Fig. 7 The macroscopic stress–strain curves and fracture surfaces of the tested specimens under a tensile load

In the stress–strain curve of the T2 specimen, five loading states, as shown in Fig. 8 (a), were selected to study the damage evolution. Fig. 8 (b) depicts the strain distribution along one line of the T2 specimen in the tensile direction for five loading states. In the initial state, the tensile strain along the line was uniformly distributed. With an increase in tensile load, strain concentrations occurred at certain locations,

and the stress–strain response was linear up to the PLS, followed by a nonlinear region of decreasing tangent modulus, culminating in failure. In the subsequent states, the strain concentrations at certain locations increased significantly. Fig. 8 (c) shows the surface states at the selected loading states. Several macroscopic cracks were observed, and the cracking at these locations appears as a strain concentration due to the step change in displacement across the crack. The coloured dotted oval represents the crack evolution. Owing to differences in the capacity of the matrix to resist cracking at different locations, some cracks remained stable, whereas others grew, observed as significant strain concentrations. Fig. 8 (d) shows the strain distribution at selected loading states. After the stress reached the PLS, a band of strain concentration on the specimen surface appeared along the crack. After the three states, the stress–strain curve again showed nonlinearity. As indicated by Fig. 8 (c) and (d), the macroscopic cracks in the T2 specimen tended to be saturated.

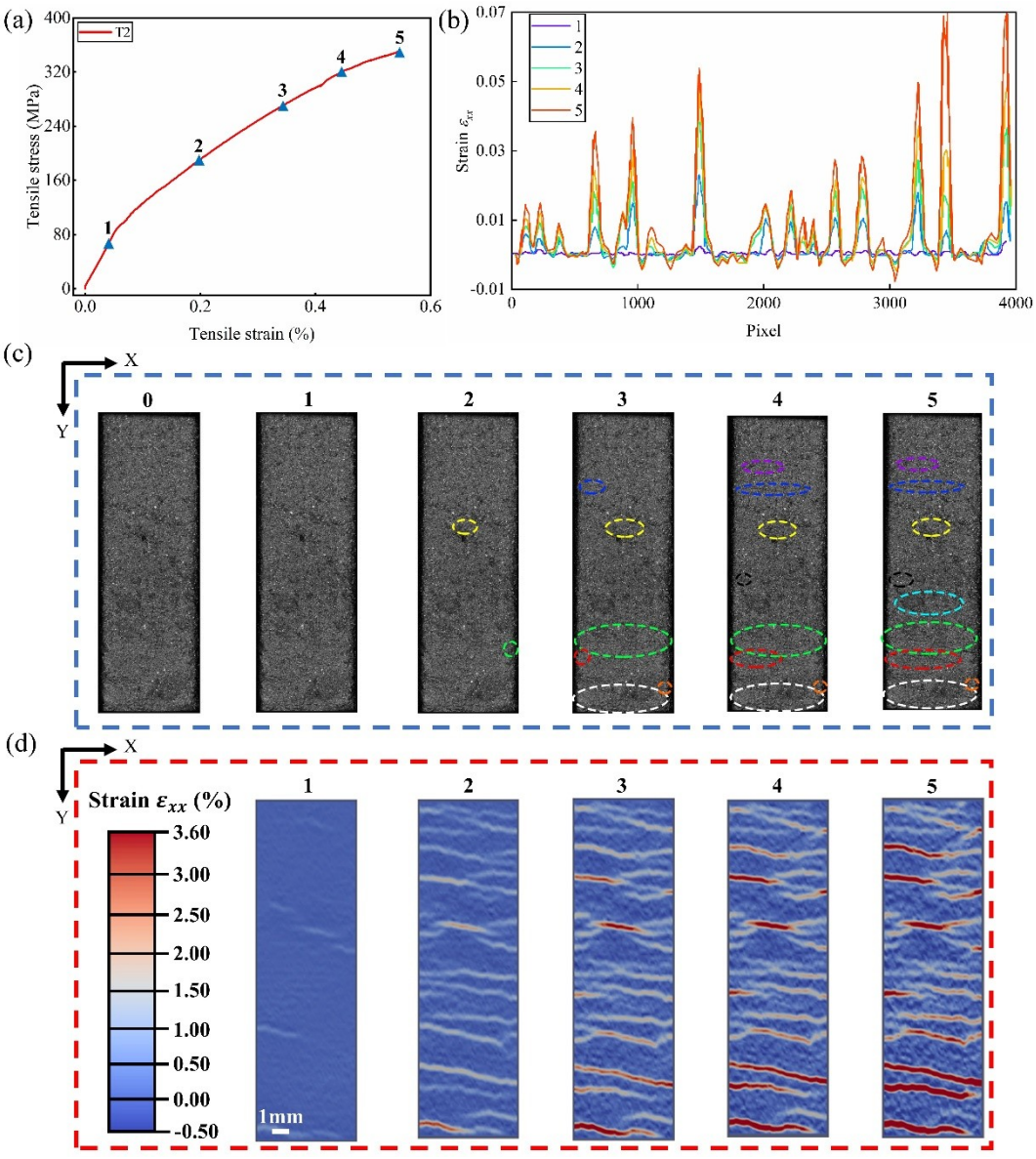


Fig. 8 Experimental damage evolution of T2 specimen with increasing tensile load at room temperature. (a) The selection of five loading states, (b) strain distribution along one line in the tensile direction, (c) the surface states and (d) the strain distribution

Based on the experimental data of the feature specimens (that is, TH1, TH2, TH3, and TH4), as indicated by Fig. 9 (a), the 3D4d braided SiC/SiC composites were insensitive to notches, implying good toughness of the structural components made by

the composites. Similarly in the stress–strain curve of the TH1 specimen, five loading states were selected, as shown in Fig. 9 (b). As shown in Fig. 9 (c) and (d), most macroscopic cracks and serious strain concentrations, which are due to cracking, were distributed beside the centre hole, and these led to the ultimate failure.

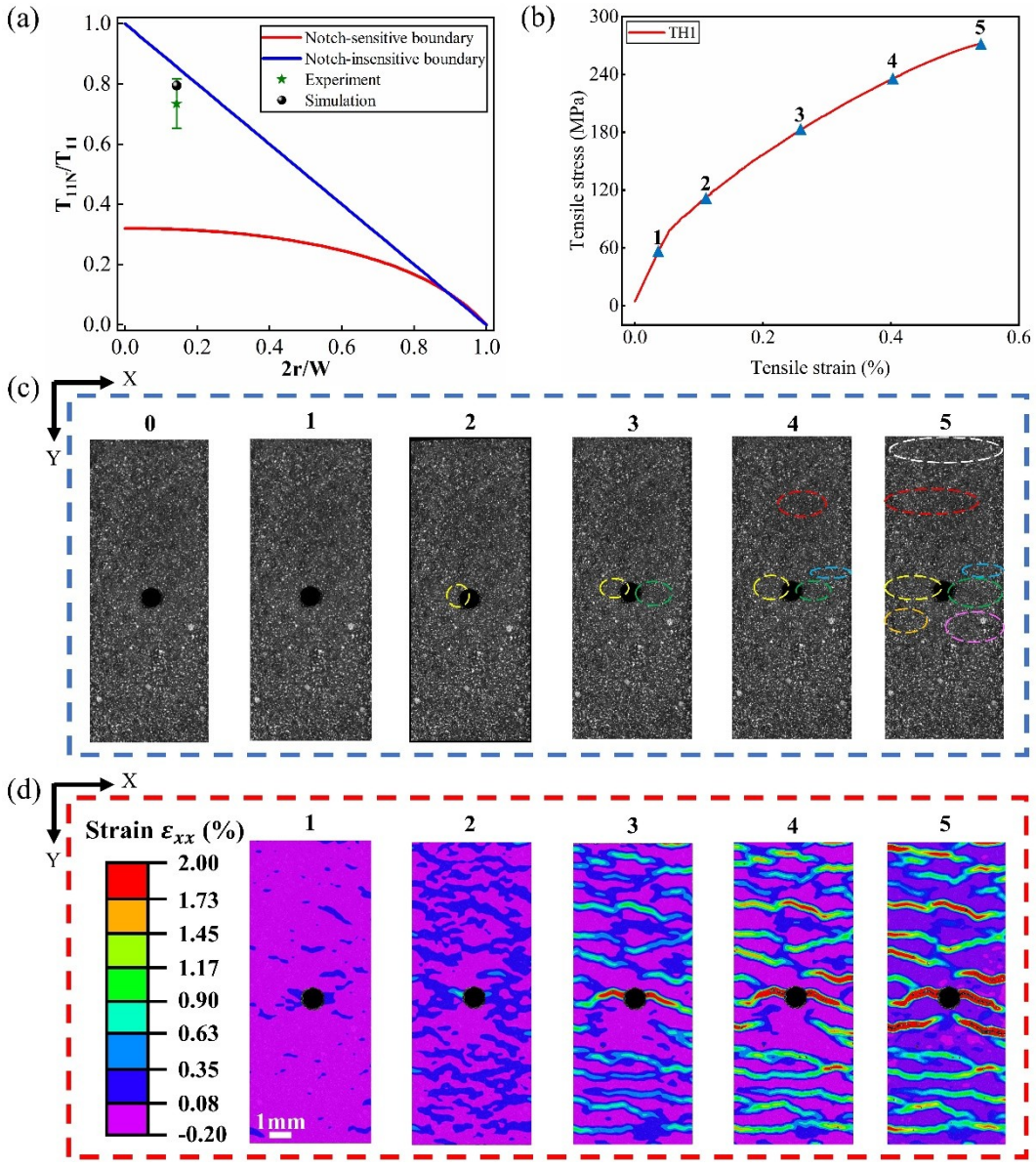


Fig. 9 (a) Notch sensitivity of SiC/SiC composites. Experimental damage evolution of TH1 specimen with increasing tensile load at room temperature. (b) The selection of five loading states, (c) the surface states and (d) the strain distribution

Fig. 10 shows the failure modes of the tested specimens observed with X-CT after loading. Several microscopic types of damage, namely, inter bundle debonding, fibre breakage, and intra bundle cracking, caused the growth of macroscopic cracks and nonlinearity of the stress–strain curves. After failure, the damaged specimen was reconstructed using X-CT and the fracture surface was also observed using SEM. Fig. 11 shows the results of the damage inspection at the fracture surfaces of the tested specimens. For standard specimens, the location of the crack initiation was at the edge, and for feature specimens, the location was adjacent to the centre hole. The SEM images showed that the fracture surface was rough, and fibre pull-outs occurred in most areas. Inter bundle debonding, fibre breakage, interface slip and debonding, and intra bundle cracking were the major failure modes. Notably, the ultimate failure of the tested specimens was related to continuous fibre breakage. Additionally, based on the fracture surfaces of the fibres, fibre breakage occurred mainly owing to longitudinal loading; this was consistent with the assumption of the selection of the damage initiation criterion of fibres.

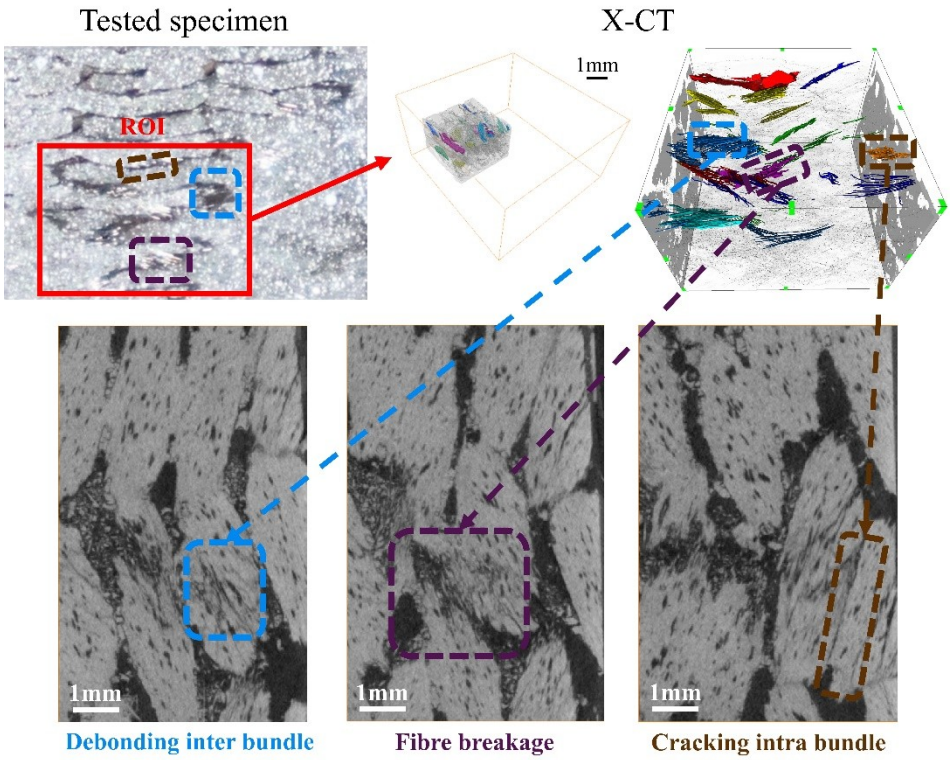


Fig. 10 Failure modes of the tested specimen after loading with X-CT

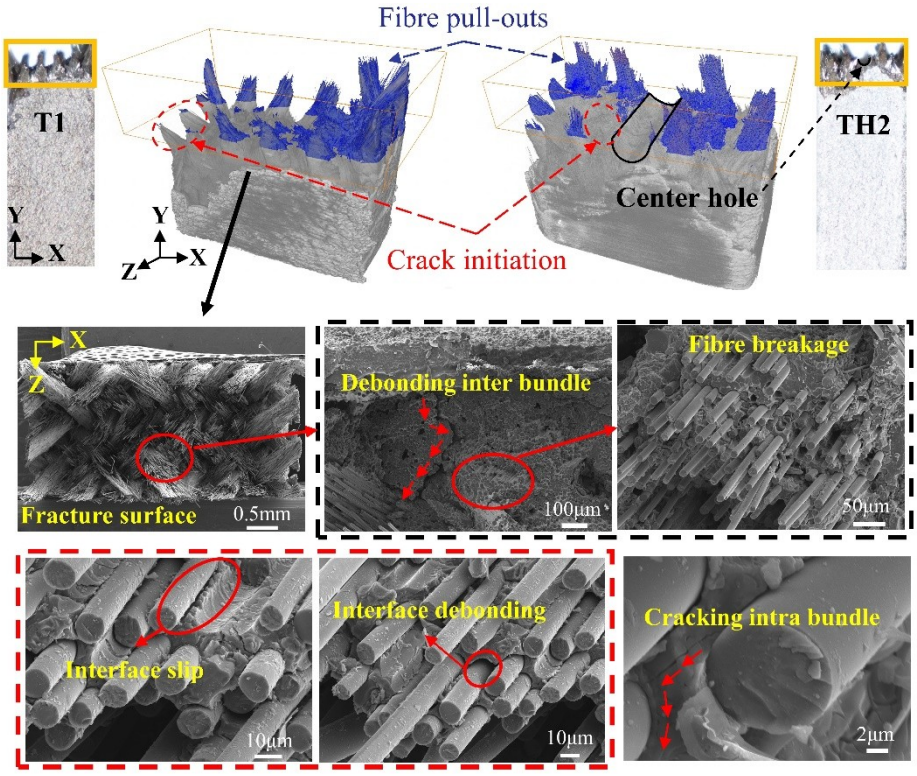


Fig. 11 Damage inspection with X-CT and SEM at the fracture surfaces of the tested specimens

4.2 Simulation results

4.2.1 Microscopic simulation

Fig. 12 shows the simulated stress–strain curves and stress distributions in the linear segment under various loading modes. In the longitudinal direction of the fibre bundles, the tensile modulus was 195.6GPa, and tensile and compressive strengths were 1682.6MPa and 1212.3MPa, respectively. In the transverse direction, the tensile modulus is 165.2GPa, and tensile and compressive strengths were 83.6MPa and 170.5MPa, respectively. Under 1-2 shear loading, the modulus was 69.3GPa, and the strength was 61.6MPa. Under 2-3 shear loading, the modulus was 67.9GPa, and the strength was 56.2MPa. The longitudinal properties of the fibre bundles were

significantly superior to their transverse and shear properties. This distinction between fibre bundles in various directions originated from the differences in the main load-bearing components and specific failure modes under various loading modes.

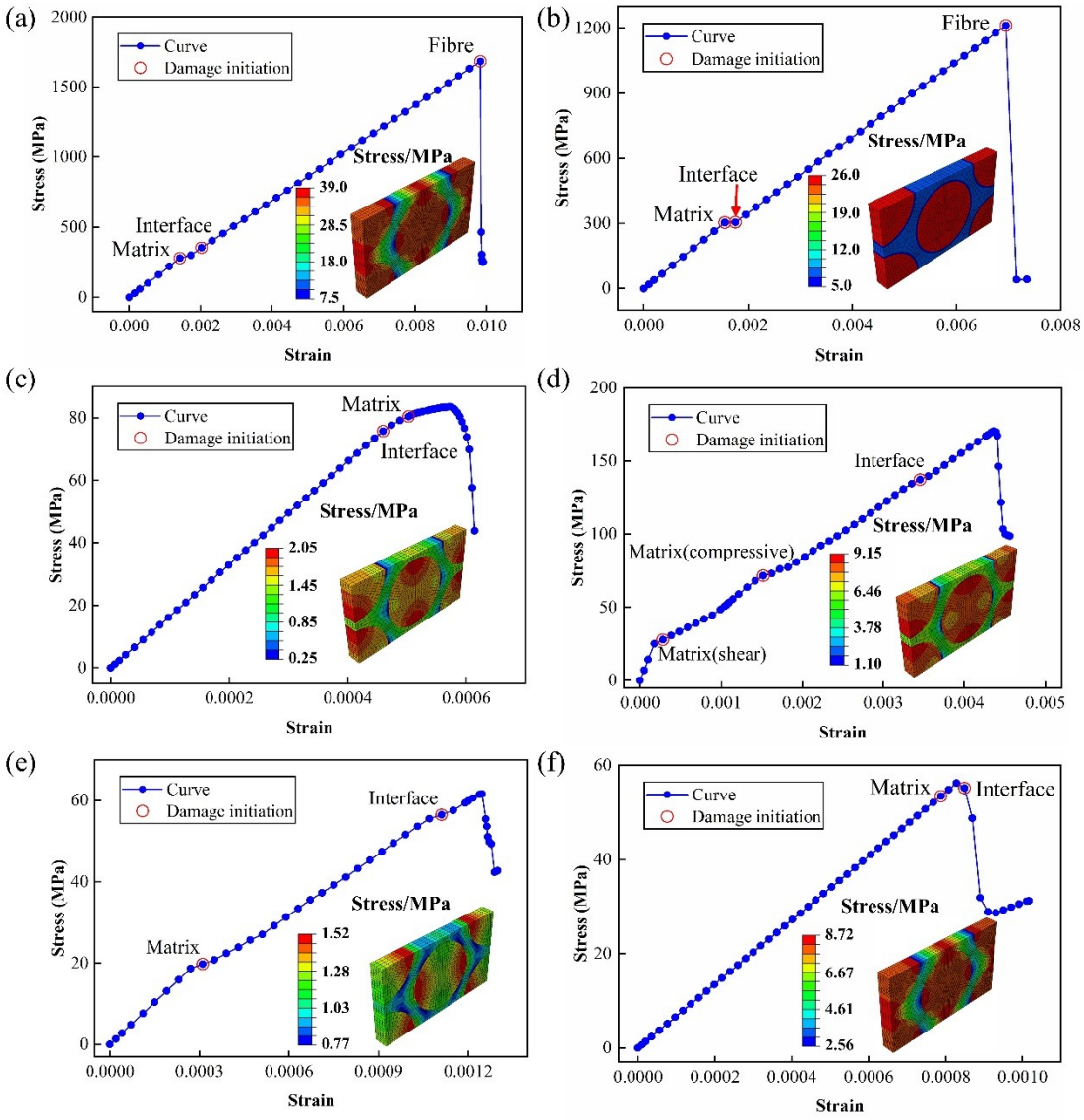


Fig. 12 Simulated stress–strain curves with damage evolution and stress distribution in the linear segment under (a) longitudinal tensile load, (b) longitudinal compressive load, (c) transverse tensile load, (d) transverse compression load, (e) 1–2 shear load and (f) 2–3 shear load

Fig. 13 depicts the failure behaviour of the fibre bundles under various loading modes. With increasing longitudinal tensile load, first, matrix tensile damage occurred and caused nonlinearity in the stress–strain curve. Second, interface damage occurred. Finally, the fibre bundle lost its load-bearing capacity, and brittle fractures occurred owing to fibre tensile damage. Under longitudinal compressive loading, matrix shear damage occurred first, followed by interface and fibre compressive damage. Based on the stress distribution and failure modes in the longitudinal direction of the fibre bundles, the main load-bearing component was the fibre, whose damage dominated the ultimate failure. With an increase in the transverse tensile load, interface damage occurred first, followed by matrix tensile and shear damage. As the matrix damage tended to saturate, the fibre bundle lost its load-bearing capacity. Under transverse compressive loading, matrix shear and compressive damage occurred first, and interface damage finally occurred. With an increase in the 1-2 shear load, matrix shear damage occurred first, and interface shear damage finally occurred. Particularly under 2-3 shear loading, no damage occurred before reaching the ultimate stress, and matrix and interface damage occurred instantly at the ultimate stress state. This shows that when selecting the damage initiation criterion and damage evolution law for fibre bundles, the clear distinctions between failure modes under various loading modes must be considered.

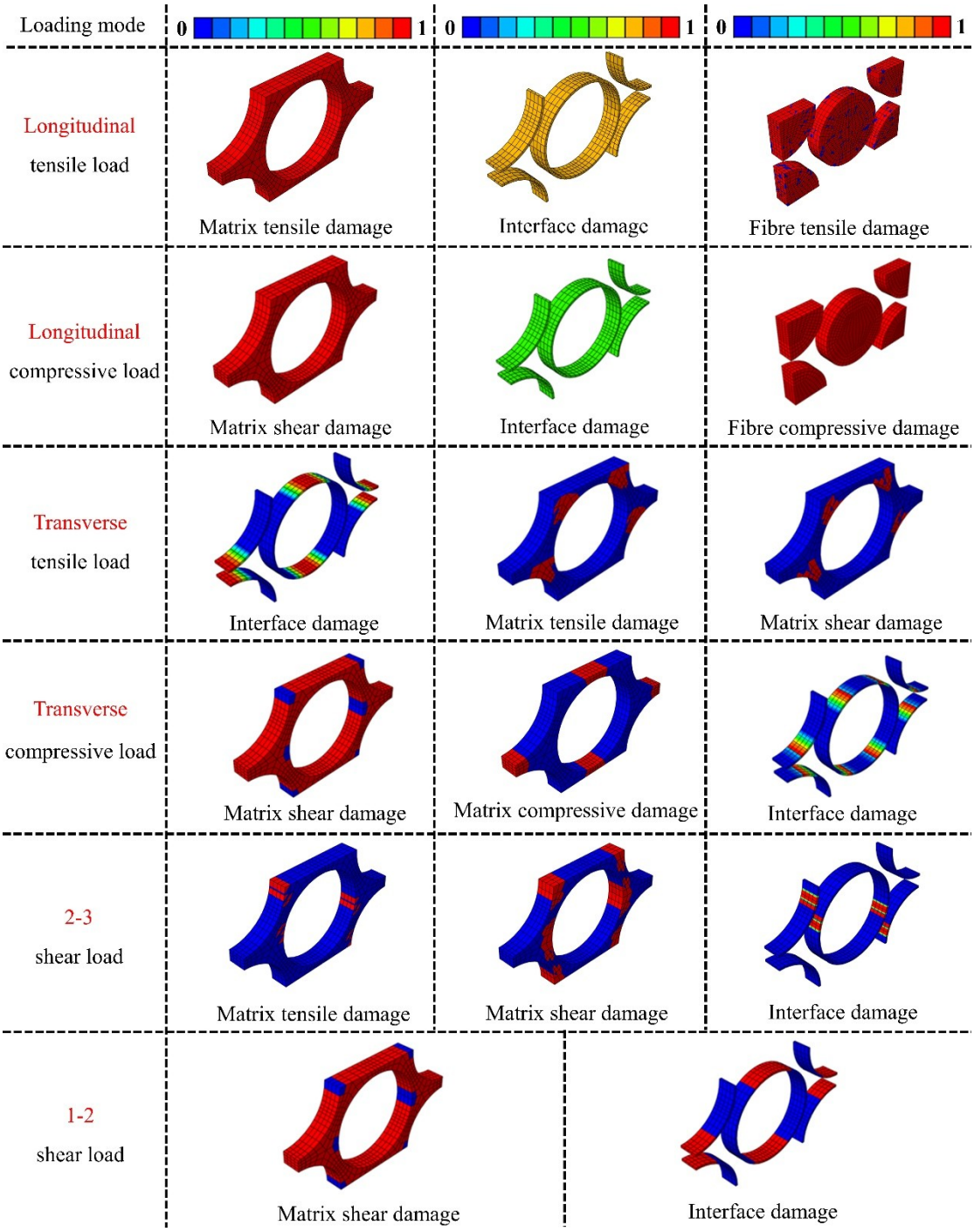


Fig. 13 The failure behaviour of the fibre bundles under various loading modes

The modulus and strength of the fibre bundle are typically calculated using the Chamis formula described in Eqs. (37) and (38), respectively:

$$E_{11} = V_{fib} \cdot E_{f11} + (1 - V_{fib}) \cdot E_{mp}$$

$$E_{22} = E_{33} = \frac{E_{mp}}{1 - \sqrt{V_{fib}} \left[1 - E_{mp} / E_{f22} \right]}$$

$$G_{12} = G_{13} = \frac{E_{mp}}{2 \cdot (1 + \nu_m) - \sqrt{V_{fib}} \cdot \left[2 \cdot (1 + \nu_m) - E_{mp} / G_{f12} \right]}$$

$$G_{23} = \frac{E_{mp}}{2 \cdot (1 + \nu_m) - \sqrt{V_{fib}} \cdot \left[2 \cdot (1 + \nu_m) - E_{mp} / G_{f23} \right]}$$

$$\nu_{12} = \nu_{13} = V_{fib} \cdot \nu_{f12} + (1 - V_{fib}) \cdot \nu_m$$

$$\nu_{23} = \frac{E_{22}}{2 \cdot G_{23}} - 1$$

(3838* MERGEFORMAT ())

$$T_{11} = V_{fib} \cdot T_{f11} + (1 - V_{fib}) \cdot T_{mp}$$

$$C_{11} = V_{fib} \cdot C_{f11} + (1 - V_{fib}) \cdot C_{mp}$$

$$T_{22} = \left[1 - \left(\sqrt{V_{fib}} - V_{fib} \right) \cdot \left(1 - \frac{E_{mp}}{E_{f22}} \right) \right] \cdot T_{mp}$$

$$C_{22} = \left[1 - \left(\sqrt{V_{fib}} - V_{fib} \right) \cdot \left(1 - \frac{E_{mp}}{E_{f22}} \right) \right] \cdot C_{mp}$$

$$S_{12} = \left[1 - \left(\sqrt{V_{fib}} - V_{fib} \right) \cdot \left(1 - \frac{G_{mp}}{G_{f12}} \right) \right] \cdot S_{mp}$$

$$S_{23} = \frac{\left[1 - \sqrt{V_{fib}} \cdot \left(1 - G_m / G_{f23} \right) \right] \cdot S_{mp}}{1 - V_{fib} \cdot \left(1 - G_m / G_{f23} \right)}$$

(3939* MERGEFORMAT ())

where *T*, *C*, and *S* denote the tensile, compressive, and shear strengths of the basic components of the fibre bundles, respectively. Table 4 presents a comparison between the simulation and calculation results using the Chamis formula and indicates good

consistency. The main errors between the simulation and calculation results originated from ignoring the interface influence in the Chamis formula. In particular, large relative errors existed in the shear strengths that were related to interface damage, leading to ultimate failure under shear loading of the fibre bundles.

Table 4 The comparison between the simulation and calculation results using Chamis formula about elastic parameters and strength of fibre bundles

Elastic parameter	Simulation results	Chamis formula	Relative error
E_{11}(GPa)	195.6	197.9	1.2%
E_{22}(GPa)	165.2	183.4	9.9%
G_{12}(GPa)	69.3	73.8	6.1%
G_{23}(GPa)	67.9	73.8	8.0%
v_{12}	0.228	0.235	3.0%
v_{23}	0.266	0.243	9.5%
Strength	Simulation results	Chamis formula	Relative error
T_{11}(MPa)	1682.6	1664.9	1.1%
C_{11}(MPa)	1212.3	1249.8	3.0%
T_{22}(MPa)	83.6	102.0	18.0%
C_{22}(MPa)	170.5	204.1	16.5%
S_{12}(MPa)	61.6	50.8	21.3%
S_{23}(MPa)	56.2	45.4	23.8%

4.2.2 Mesoscopic simulation

In Fig. 14 (a), the simulated stress–strain curves with damage evolution are compared with the experimental curves of the standard specimens. Matrix shear damage led to the initial nonlinearity of the stress–strain curves of the SiC/SiC composites. The simulated PLS was approximately 110.1MPa that was slightly higher than the experimental data of 86.1MPa. Matrix tensile damage, matrix-dominated bundle damage, and fibre-dominated bundle damage occurred sequentially with an increase

in the longitudinal tensile load. The simulated UTS was 336.2MPa, which was close to the experimental data of 332.5MPa. The simulated tensile modulus was 123.1GPa, which was less than the experimental data of 136.9GPa. The moduli of the surface and corner RVEs were larger than those of the interior RVEs, causing a smaller modulus in the simulation results based on the interior RVEs compared with the experimental data. Fig. 14 (b) shows the simulated displacement and stress distribution in the linear segment. This indicated that the primary load-bearing component was the fibre bundle.

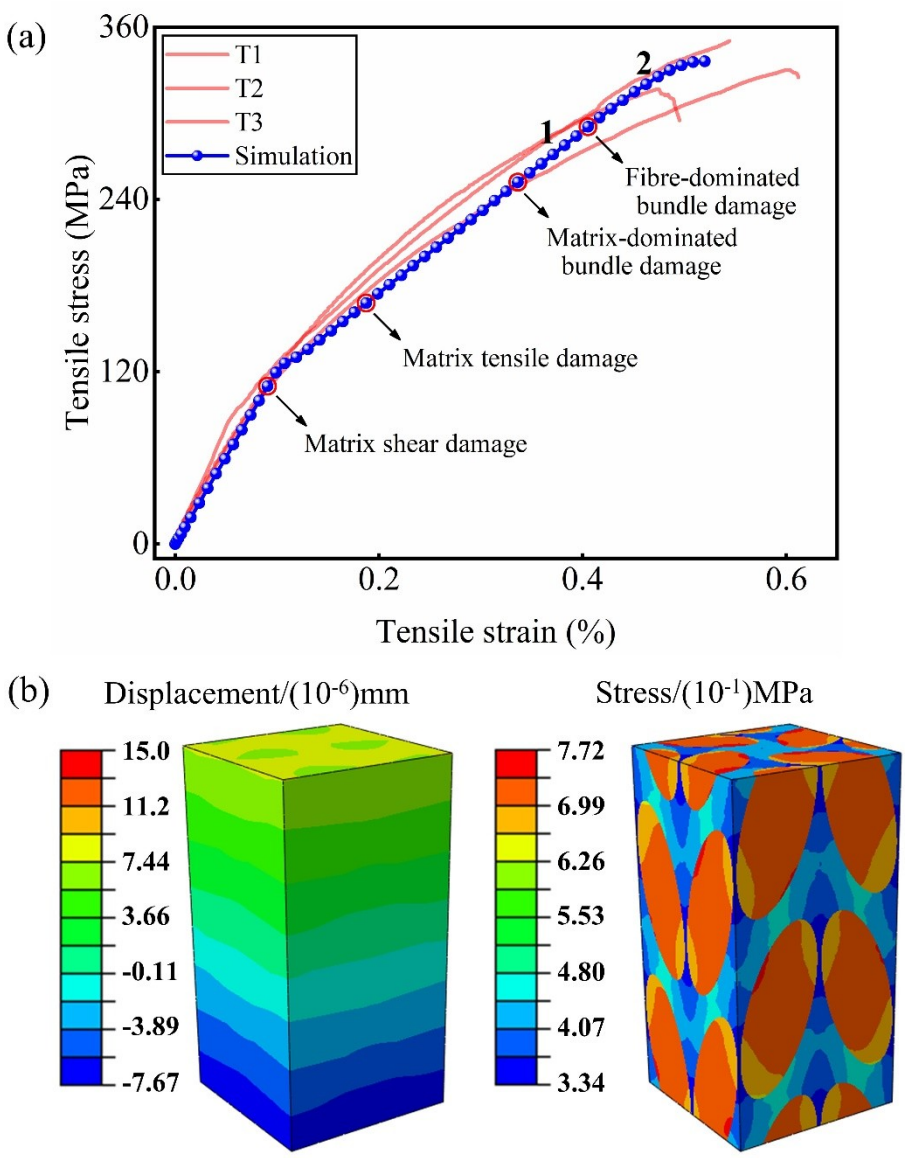


Fig. 14 Under longitudinal tensile loading, (a) stress-strain curves with damage evolution, (b) simulated displacement and stress distribution in the linear segment

Four loading states (that is, 1, 2, peak stress, and after failure) were selected in the simulated stress–strain curve. Fig. 15 displays the damage distribution at the four loading states. The proportion of damaged elements is defined as the ratio of the number of damaged elements to the number of constitutive elements. Fig. 16 shows the simulated damage variable evolution of the typical elements and proportion

evolution of the damaged elements of the main failure modes under longitudinal tensile loading. The damaged elements were categorised based on their damage variable values.

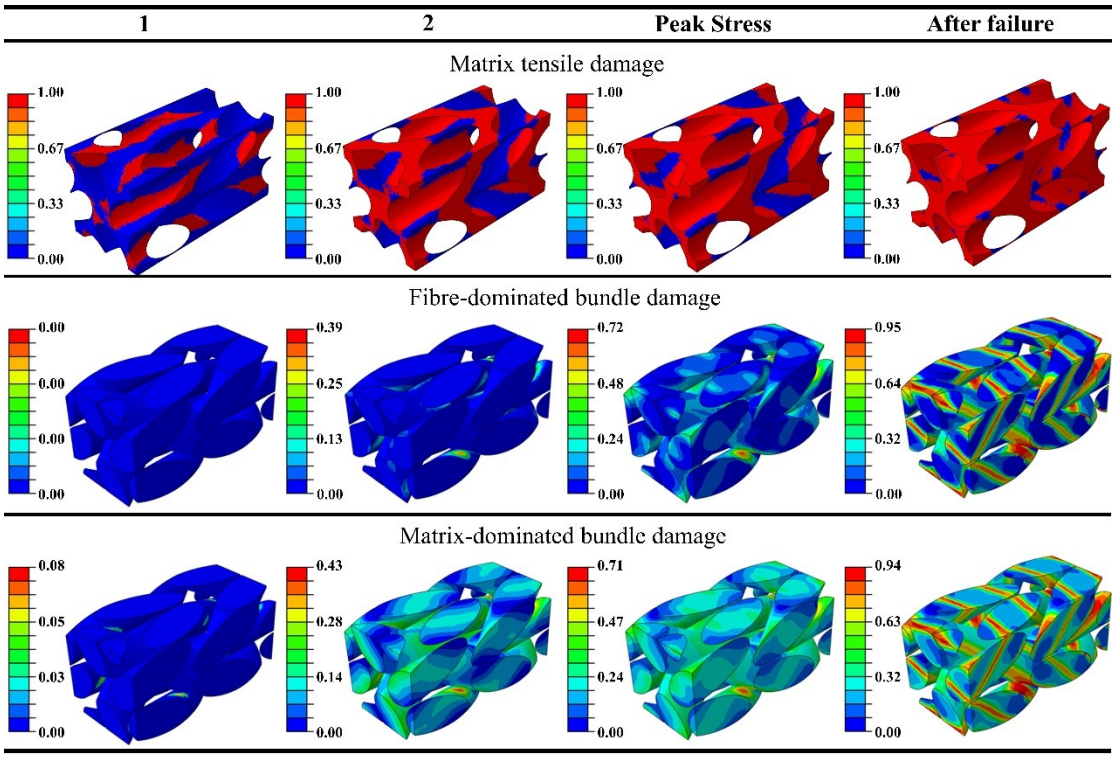


Fig. 15 Damage distribution at the four loading states

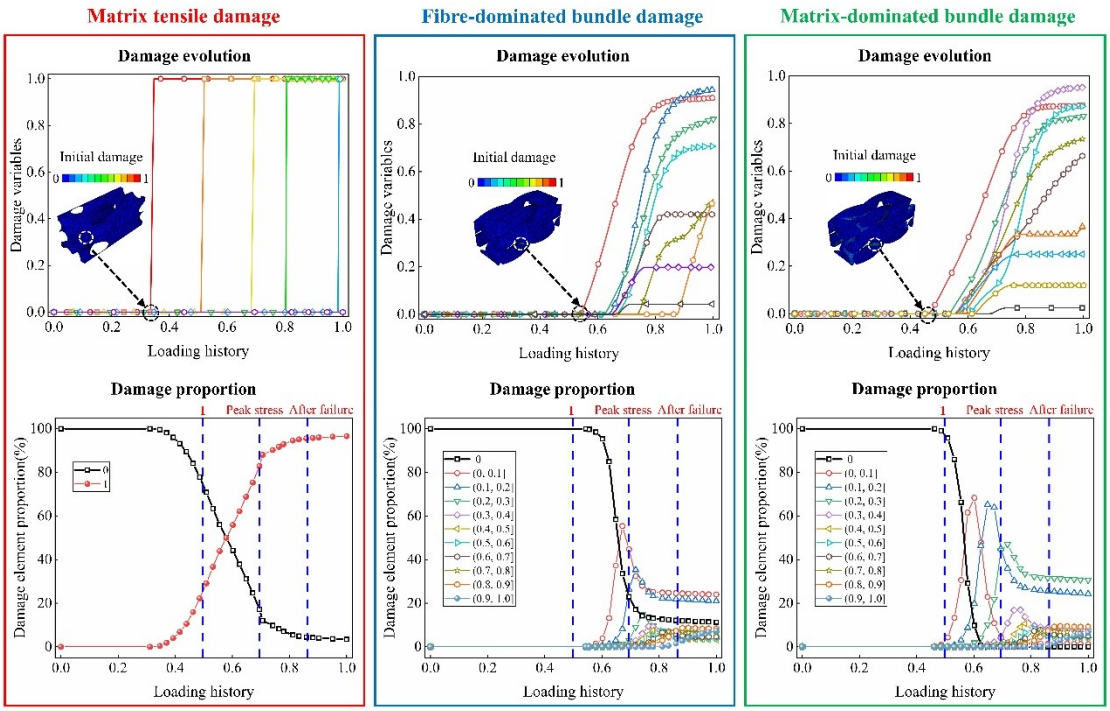


Fig. 16 Simulated damage variable evolution of the typical elements and proportion evolution of the damaged elements of the main failure modes under longitudinal tensile loading

First, matrix damage occurred near the contact region of the fibre bundles, and extensive matrix tensile damage occurred as the loading continued. Subsequently, near the contact region of the matrix, transverse matrix-dominated bundle damage occurred in the 1 state. The fibre bundles exhibited transverse fibre-dominated damage. With an increase in the longitudinal tensile load, extensive bundle damage occurred along the longitudinal direction. Near the peak stress state, fibre-dominated bundle damage propagated rapidly. Eventually, the fibre-dominated bundle damage caused the ultimate failure of the composites; this was consistent with the experimental observations. After failure, the major matrix and fibre bundle elements suffered tensile damage and fibre-dominated bundle damage, respectively. In

particular, matrix-dominated bundle damage occurred in all elements of the fibre bundles. This analysis indicates that the proposed damage model possesses the ability to provide reliable predictions of the mechanical properties and strength and reflected the realistic damage mechanisms of SiC/SiC composites.

4.2.3 Macroscopic simulation

Fig. 17 (a) illustrates the simulated and experimental stress–strain curves of the feature specimens. The simulated UTS was 264.2MPa, and the relative errors of the UTS between the simulation and the experiments was 8.2%. Four loading stages were selected in the simulated stress–strain curve. Fig. 17 (b) shows the damage distribution at the selected loading stages. In the first stage (1), matrix damage occurred and caused a turning point in the stress–strain curve. At the edge of the centre hole and specimen, the stress state in many regions reached the PLS of the SiC/SiC composites. After the first stage, second-level damage occurred at the edge of the centre hole. As the load increased, the damaged regions developed into the shape of a hyperbola. When the damaged elements joined together at the cross-section of the specimen, the ultimate failure occurred. The fracture surface location of the TH1 specimen matched the failure regions in the simulation. Fig. 18 shows the strain fields of the feature specimens of the simulation and in-situ experimental results in the linear segment. The consistency between the simulated and measured strain fields at the edge of the centre hole confirmed that the proposed damage model could calculate the complex strain distribution of the feature specimens.

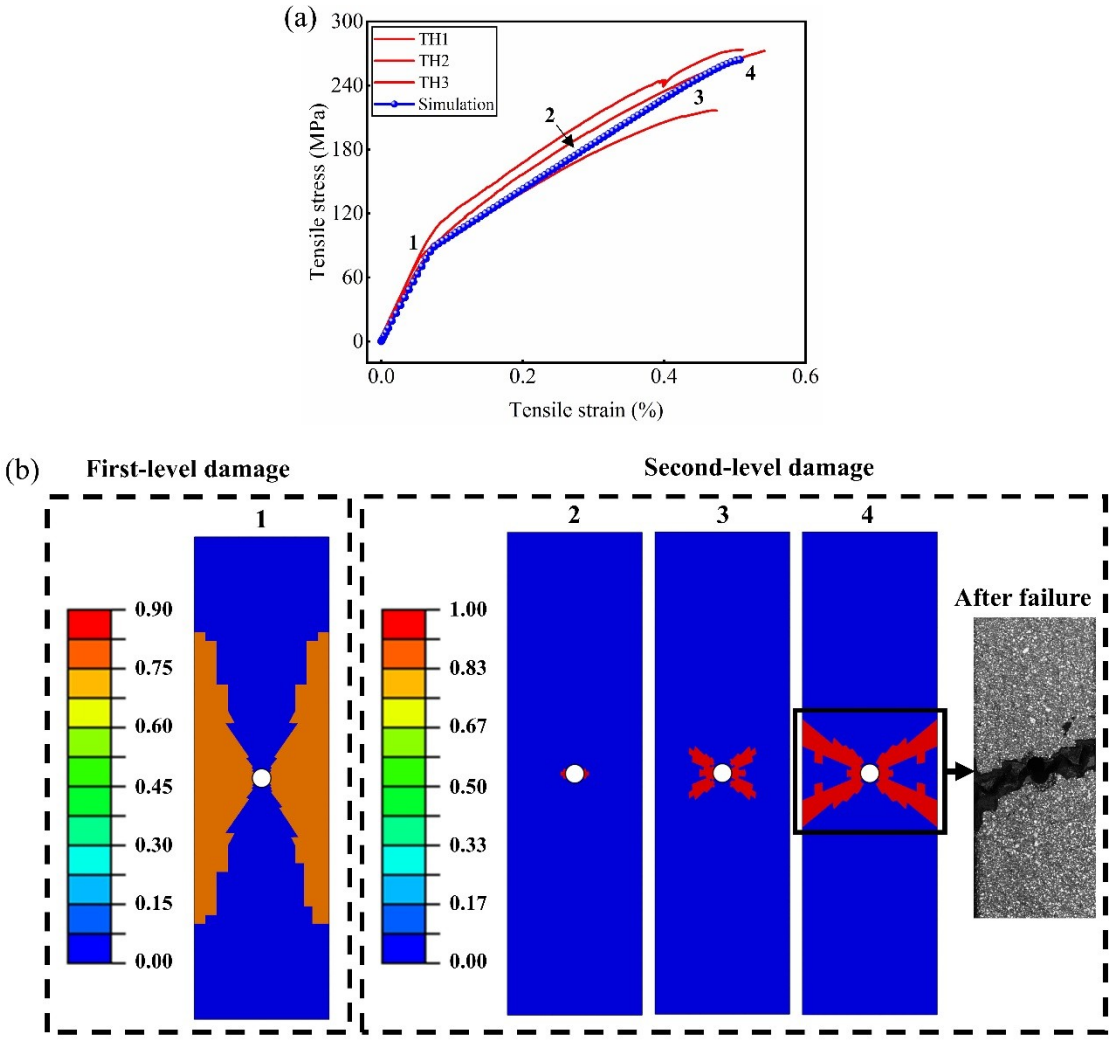


Fig. 17 Under longitudinal tensile loading, (a) stress-strain curves of feature specimens and (b) simulated damage evolution in two levels

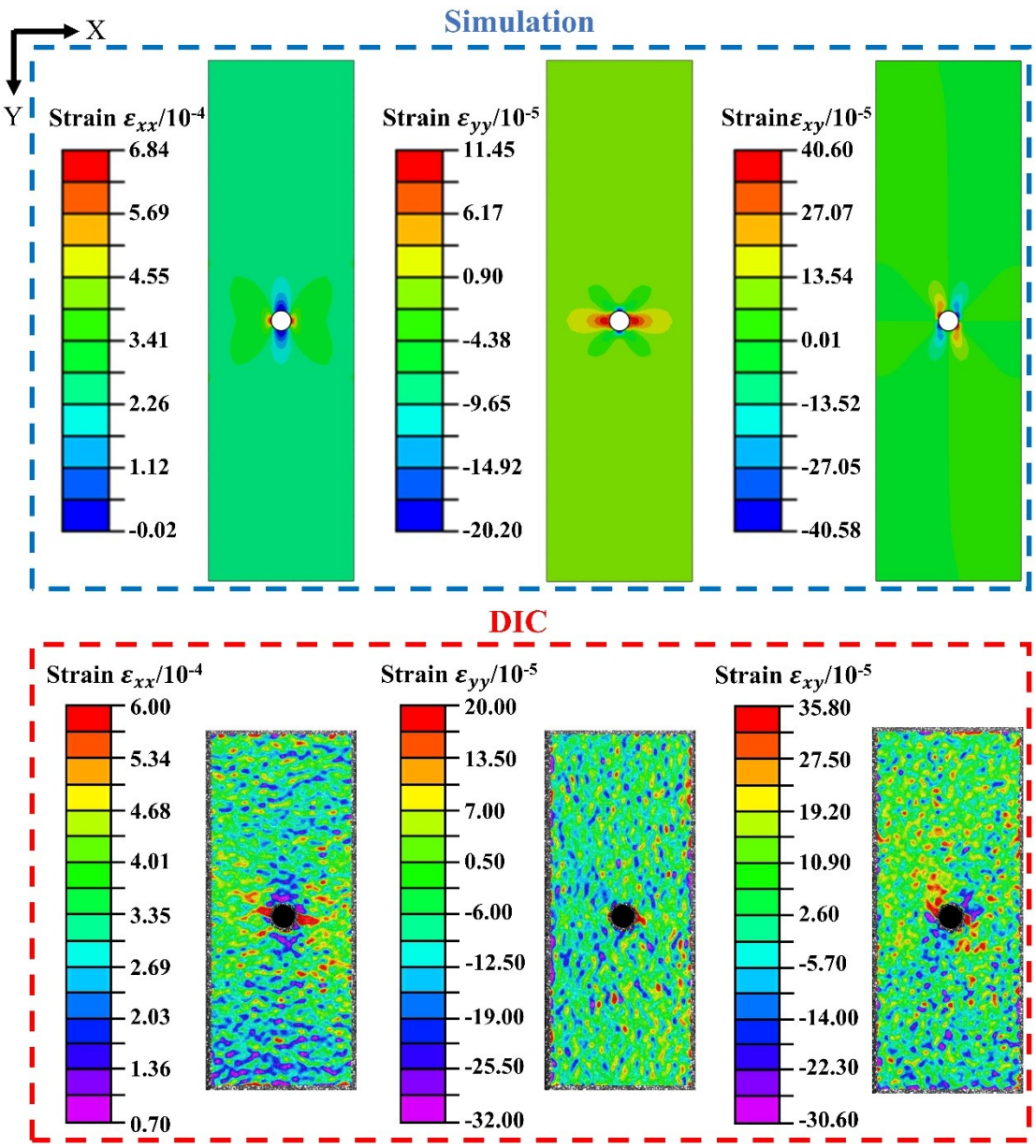


Fig. 18 The strain fields of the feature specimens of the simulation and in-situ experimental results in the linear segment

Fig. 19 shows the predicted radial stress field, first-level damage distribution, and tensile test results for the SiC/SiC composite blade. Under centrifugal loading, the radial tensile stress was the primary stress in the blade body, and the stress concentrated at the root of the blade back. The first-level damage occurred in many

elements of the blade back, and serious damage mainly occurred at the blade root section; this was consistent with the location of the fracture surface in the tensile tests of the SiC/SiC composite blade.

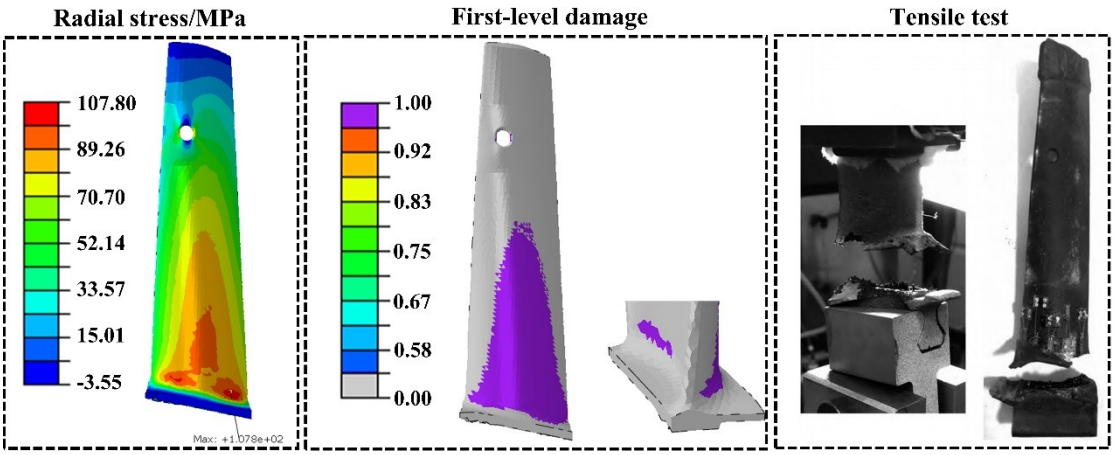


Fig. 19 The simulation and test results for the structural component of SiC/SiC composites

5. Conclusion

Referring to multiscale and multidimensional data from accurate in-situ experiments and advanced microscopic characterisation techniques, a piecewise damage model for multilevel SiC/SiC composite structures was proposed. The elastic and strength properties, deformation and stress fields, and damage evolution in multilevel structures of SiC/SiC composites were investigated, and the in-situ experimental results validated the reliability of the modelling method. Several significant conclusions can be drawn.

First, by importing multilevel structures and material parameters of SiC/SiC composites into the PFA, the damage mechanisms of SiC/SiC composites were

modelled at multiple scales. For fibre bundles, the longitudinal properties depended on the fibres, whereas the transverse properties were determined by the matrix and interface. In composites, fibre-dominated bundle damage rapidly propagated and this caused the ultimate failure near the peak stress state.

Subsequently, accurate in-situ experiments and advanced microscopic characterisation were conducted to observe the microstructures, defects, deformation, and failure behaviour of the SiC/SiC composites. The displacement field calculated using DIC was shown to be reliable, and the observed strain concentrations revealed the growth of macroscopic cracks. Debonding inter bundle, fibre breakage, interface slip and debonding, and cracking intra bundle were the major failure modes of the SiC/SiC composites. The ultimate failure was related to continuous fibre breakage.

Ultimately, by combining reliable piecewise damage modelling and advanced testing methods, the deformation and failure behaviour of SiC/SiC composite structures could be predicted. These modelling and testing methods will serve as a foundation for the design and strength assessment of SiC/SiC composite structures.

Acknowledgements

This work was supported by the National Natural Science Foundation of China (51772009 and 51911530201) and the Postdoctoral Research Foundation of China (2022M720352). The use of X-CT facilities funded by EPSRC Grant EP/M02833X/1 “University of Oxford: experimental equipment upgrade” is gratefully acknowledged.

Author Credit

Duoqi Shi: Conceptualization, Supervision, Funding acquisition, **Zhenyu Wang:** Investigation, Visualization, Writing – original draft, **Changqi Liu:** Investigation, Methodology, Writing – review and editing, **James Marrow:** Supervision, Writing – review and editing, **Xiaoguang Yang:** Project administration.

References

[1] Liu, D., et al., Current status and development direction of aircraft power technology in the world. Journal of Beijing University of Aeronautics and Astronautics, 2002. 28(5): p. 490-496.

[2] Liu, C., et al., A novel creep-fatigue life evaluation method for ceramic-composites components. International Journal of Mechanical Sciences, 2023. 249: p. 108259.

[3] Chen, M. and Q. Liu, Multi-scale modelling of progressive damage and failure behaviour of 2D woven SiC/SiC composites. Ceramics International, 2021. 47(20): p. 28821-28836.

[4] Santhosh, U., et al., Deformation and damage modeling of ceramic matrix composites under multiaxial stresses. Composites Part B: Engineering, 2016. 90: p. 97-106.

[5] Wang, X., et al., Advances in modifications and high-temperature applications of silicon carbide ceramic matrix composites in aerospace: A focused review. Journal of the European Ceramic Society, 2021. 41(9): p. 4671-4688.

[6] Sciti, D., et al., A systematic approach for horizontal and vertical scale up of sintered Ultra-High Temperature Ceramic Matrix Composites for aerospace – Advances and perspectives. Composites Part B: Engineering, 2022. 234: p. 109709.

[7] Shi, D. et al., Conceptual design of ceramic matrix composites turbine blade for typical turbofan engine. Journal of Aerospace Power, 2023. 38(02): p. 431-444.

[8] Genet, M., et al., Computational prediction of the lifetime of self-healing CMC structures. Composites Part A: Applied Science and Manufacturing, 2012. 43(2): p. 294-303.

[9] Naslain, R., Design, preparation and properties of non-oxide CMCs for application in engines and nuclear reactors: an overview. Composites Science and Technology, 2004. 64(2): p. 155-170.

[10] Schmidt, S., et al., Advanced ceramic matrix composite materials for current and future propulsion technology applications. Acta Astronautica, 2004. 55(3-9): p. 409-420.

[11] Patel, A., et al., Effect of oxidation on the bending fatigue behavior of an advanced SiC/SiC CMC component at 1000 °C in air. Journal of the European Ceramic Society, 2022. 42(10): p. 4121-4132.

[12] Meyer, P. and A.M. Waas, Experimental results on the elevated temperature tensile response of SiC/SiC ceramic matrix notched composites. Composites Part B: Engineering, 2018. 143: p. 269-281.

[13] Morscher, G.N. and R. Maxwell, Monitoring tensile fatigue crack growth and fiber failure around a notch in laminate SIC/SIC composites utilizing acoustic emission, electrical resistance, and digital image correlation. Journal of the European Ceramic Society, 2019. 39(2-3): p. 229-239.

[14] Delage, J., E. Saiz and N. Al Nasiri, Fracture behaviour of SiC/SiC ceramic matrix composite at room temperature. Journal of the European Ceramic Society, 2022. 42(7): p. 3156-3167.

[15] Gao, X., et al., Failure analysis of C/SiC composites plate with a hole by the PFA and DIC method. Ceramics International, 2017. 43(6): p. 5255-5266.

[16] Skinner, T. and A. Chattopadhyay, Multiscale temperature-dependent ceramic matrix composite damage model with thermal residual stresses and manufacturing-induced damage. Composite Structures, 2021. 268: p. 114006.

[17] Wei, Y., et al., Effects of in-situ carbon layer and volume fraction of SiC fiber on the mechanical properties and fracture behaviors of SiCf/SiC composites

fabricated by a modified PIP method. Journal of the European Ceramic Society, 2023. 43(4): p. 1397-1406.

[18] Bernachy-Barbe, F., et al., Characterization of SiC/SiC composites damage mechanisms using Digital Image Correlation at the tow scale. Composites Part A: Applied Science and Manufacturing, 2015. 68: p. 101-109.

[19] Zhang, D., et al., Characterisation of damage evolution in plain weave SiC/SiC composites using in situ X-ray micro-computed tomography. Composite Structures, 2021. 275: p. 114447.

[20] Dongcheng Han, Ye Fang, Cheng Laifei, et al. Matrix cracking of 2D SiC/SiC composite characterized by in situ SEM and nano-CT[J]. Ceramics International, 2023, 49(8): 12508-12517.

[21] Maillet, E., et al., Combining in-situ synchrotron X-ray microtomography and acoustic emission to characterize damage evolution in ceramic matrix composites. Journal of the European Ceramic Society, 2019. 39(13): p. 3546-3556.

[22] Liu, C., et al., In situ investigation of failure in 3D braided SiCf/SiC composites under flexural loading. Composite Structures, 2021. 270: p. 114067.

[23] Shi, D., et al., In-situ study on compressive behaviors of different types of 3D SiC/SiC composites using X-ray computed tomography and digital image correlation. Journal of Materials Research and Technology, 2023. 22: p. 3475-3488.

[24] Zhao, S., et al., Hoop Strain Measurement During a SiC/SiC Ceramic Composite Tube Burst Test by Digital Volume Correlation of X-Ray Computed Tomographs. Experimental Mechanics, 2023. 63(2): p. 275-287.

[25] Saucedo-Mora, L., et al., Multi-scale damage modelling in a ceramic matrix composite using a finite-element microstructure meshfree methodology. Philosophical Transactions of the Royal Society of London A: Mathematical, Physical and Engineering Sciences, 2016. 374(2071).

[26] Saucedo-Mora, L., et al., In situ observation of mechanical damage within a SiC-SiC ceramic matrix composite. Journal of Nuclear Materials, 2016. 481: p. 13-23.

[27] Quiney, Z., et al., Volumetric assessment of fatigue damage in a SiCf/SiC ceramic matrix composite via in situ X-ray computed tomography. Journal of the European Ceramic Society, 2020. 40(11): p. 3788-3794.

[28] Sun, Z., et al., A multiscale modeling for predicting the thermal expansion behaviors of 3D C/SiC composites considering porosity and fiber volume fraction. Ceramics International, 2021. 47(6): p. 7925-7936.

[29] Hallal, A., R. Younes and F. Fardoun, Review and comparative study of analytical modeling for the elastic properties of textile composites. Composites Part B: Engineering, 2013. 50: p. 22-31.

[30] Wang, Z., et al., Tensile behavior and failure mechanism of 3D woven fabric reinforced aluminum composites. International Journal of Mechanical Sciences, 2023. 244: p. 108043.

[31] Zhang, Y. and Z. Zhou, Experimental and multiscale numerical investigation on failure behavior of satin woven carbon/carbon composites subjected to pin-loading. International Journal of Mechanical Sciences, 2022. 219: p. 107129.

[32] Ge, L., et al., Multiscale viscoelastic behavior of 3D braided composites with pore defects. Composites Science and Technology, 2022. 217: p. 109114.

[33] Ge, L., et al., Parametric analyses on multiscale elastic behavior of 3D braided composites with pore defects. Composite Structures, 2022. 287: p. 115332.

[34] Zheng, T., et al., Comparison of progressive damage simulation of 3D woven composites between voxel and conformal discretization models. Mechanics of Materials, 2021. 158: p. 103860.

[35] Zheng, T., et al., A novel mesoscopic progressive damage model for 3D angle-interlock woven composites. Composites Science and Technology, 2020. 185: p. 107894.

[36] Zheng, T., et al., An innovative micromechanics-based multiscale damage model of 3D woven composites incorporating probabilistic fiber strength distribution. Composite Structures, 2022. 287: p. 115345.

[37] He, C., et al., A multiscale elasto-plastic damage model for the nonlinear behavior of 3D braided composites. Composites Science and Technology, 2019. 171: p. 21-33.

[38] He, C., et al., A hierarchical multiscale model for the elastic-plastic damage behavior of 3D braided composites at high temperature. Composites Science and Technology, 2020. 196: p. 108230.

[39] He, C., et al., From microscale to mesoscale: The non-linear behavior prediction of 3D braided composites based on the SCA2 concurrent multiscale simulation. Composites Science and Technology, 2021. 213: p. 108947.

[40] Wang, B., et al., Non-orthogonal FE model with stress smoothing for progressive damage analysis of shear pre-deformed 3D angle-interlock woven composites under compression. International Journal of Mechanical Sciences, 2022. 232: p. 107642.

[41] Du, X., et al., Numerical investigation on tensile behavior of three-dimensional six-directional braided composites. International Journal of Mechanical Sciences, 2023. 237: p. 107815.

[42] Xu, S., et al., A progressive damage model for quasi-static tension of 2D woven composites and FEM implementation. Composite Structures, 2023. 320: p. 117168.

[43] Gao, Z. and L. Chen, A review of multi-scale numerical modeling of three-dimensional woven fabric. Composite Structures, 2021. 263: p. 113685.

[44] Shen, X., et al., RVE model with shape and position defects for predicting mechanical properties of 3D braided CVI-SiCf/SiC composites. Composite Structures, 2018. 195: p. 325-334.

[45] Wang, Z., et al., Real meso-scale model reconstruction and tensile failure prediction of 3D braided PIP-SiCf/SiC composites considering pore defects. Composite structures, 2023. 305.

[46] Chen, Y. and J. Marrow, Effect of irradiation swelling on the mechanical properties of unidirectional SiC/SiC composites: A numerical investigation at microstructural level. Journal of Nuclear Materials, 2022. 569: p. 153918.

[47] Ikarashi, Y., T. Ogasawara and T. Aoki, Micromechanical model of time-dependent damage and deformation behavior for an orthogonal 3D-woven SiC/SiC composite at elevated temperature in vacuum. Journal of the European Ceramic Society, 2020. 40(12): p. 3887-3896.

[48] Fu, Y., X. Yao and X. Gao, Micro-mesoscopic prediction of void defect in 3D braided composites. Composites Part A: Applied Science and Manufacturing, 2021. 147: p. 106450.

[49] Gao, X., et al., Prediction of mechanical properties on 3D braided composites with void defects. Composites Part B: Engineering, 2020. 197: p. 108164.

[50] Tang, Z., et al., A comparative study of void characteristics on the mechanical response of unidirectional composites. Mechanics of Materials, 2022. 174: p. 104456.

[51] He, J., et al., Interplay of manufacturing-induced thermal residual stresses and microvoids in damage and failure of fiber-reinforced composites. International Journal of Mechanical Sciences, 2023. 242: p. 108000.

[52] Teng, X., et al., Investigation on non-uniform strains of a 2.5D woven ceramic matrix composite under in-plane tensile stress. Journal of the European Ceramic Society, 2020. 40(1): p. 36-48.

[53] Chateau, C., et al., Micromechanical modeling of the elastic behavior of unidirectional CVI SiC/SiC composites. International Journal of Solids and Structures, 2015. 58: p. 322-334.

[54] Min, J.B., D. Xue and Y. Shi, Micromechanics modeling for fatigue damage analysis designed for fabric reinforced ceramic matrix composites. Composite Structures, 2014. 111: p. 213-223.

[55] Xu, K., A Numerical Study on the Progressive Failure of 3D Four-Directional Braided Composites. Advances in Materials Science and Engineering, 2013. 2013: p. 1-14.

[56] Ge, L., et al., Two-scale damage failure analysis of 3D braided composites considering pore defects. Composite Structures, 2021. 260: p. 113556.

[57] Omairey, S.L., P.D. Dunning and S. Sriramula, Development of an ABAQUS plugin tool for periodic RVE homogenisation. Engineering with Computers, 2019. 35(2): p. 567-577.

[58] Shi, D. et al., Structual design and static strength evalution of SiC/SiC-composite turbine blade. Journal of Aerospace Power, 2023. 38(01): p. 1-12.

[59] Chen, Y., et al., FFT phase-field model combined with cohesive composite voxels for fracture of composite materials with interfaces. Computational Mechanics, 2021. 68(2): p. 433-457.

[60] Jing, X. Investigation on high temperature mechanical behaviors of three-dimensional braided ceramic matrix composites. Beihang university, 2016.

[61] Liu, C. Analysis methods for structural strength and service life of braided SiC/SiC composites. Beihang university, 2022.

[62] Chamis C C . Simplified composite micromechanics equations for strength, fracture toughness and environmental effects. NASA Technical Memorandum, 1984. 15.

[63] Guo-dong, F., et al., The effect of yarn distortion on the mechanical properties of 3D four-directional braided composites. Composites Part A: Applied Science and Manufacturing, 2009. 40(4): p. 343-350.

[64] Hang, C., et al., Micro/meso-scale damage analysis of a 2.5D woven composite including fiber undulation and in-situ effect. Composite Structures, 2021. 256: p. 113067.

[65] Wang, Y., et al., In-plane mechanical behavior and failure mode of a 2D-SiC/SiC composite under uniaxial dynamic compression. Ceramics International, 2018. 44(16): p. 20058-20068.

[66] Tserpes, K.I., et al., Strength prediction of bolted joints in graphite/epoxy composite laminates. Composites Part B: Engineering, 2002. 33(7): p. 521-529.

[67] Tserpes, K.I. and G.N. Labeas, Mesomechanical analysis of non-crimp fabric composite structural parts. Composite Structures, 2009. 87(4): p. 358-369.

[68] McCarthy, C.T., R.M. O Higgins and R.M. Frizzell, A cubic spline implementation of non-linear shear behaviour in three-dimensional progressive damage models for composite laminates. Composite Structures, 2010. 92(1): p. 173-181.

[69] Shah, S.Z.H., et al., Multiscale damage modelling of notched and un-notched 3D woven composites with randomly distributed manufacturing defects. Composite Structures, 2023. 318: p. 117109.

[70] Huang, Z., Simulation of the mechanical properties of fibrous composites by the bridging micromechanics model. Composites Part A: Applied Science and Manufacturing, 2001. 32(2): p. 143-172.

[71] Hong, Y., et al., Mechanical behavior analysis of 3D braided composite joint via experiment and multiscale finite element method. Composite Structures, 2019. 208: p. 200-212.

[72] LIU, et al, Analysis of delamination with interface element in composite materials. Journal of Mechanical Strength, 2008.30(2): p.301~304.

[73] Z. Hashin, Failure criteria for unidirectional fiber composites, J. Appl. Mech. Trans. ASME. 47 (1980) 329–334

[74] Maimí, P., et al., A continuum damage model for composite laminates: Part II – Computational implementation and validation. Mechanics of Materials, 2007. 39(10): p. 909-919.